Preliminary investigation towards next generation truck design for aerodynamic efficiency

McAuliffe, Brian R.; Ghorbanishohrat, Faegheh; Barber, Hali

Laboratory Technical Report (National Research Council of Canada. Aerospace. Aerodynamics Laboratory); no. LTR-AL-2022-0069, 2022-07-04

UNCLASSIFIED

NRC·CNRC

AERODYNAMICS LABORATORY

Preliminary Investigation Towards Next Generation Truck Design for Aerodynamic Efficiency

LTR-AL-2022-0069

July 4, 2022

Brian R. McAuliffe, Faegheh Ghorbanishohrat, and Hali Barber

National Research Council Canada | Conseil national de recherches Canada

Canada

AERODYNAMICS LABORATORY

Preliminary Investigation Towards Next Generation Truck Design for Aerodynamic Efficiency

Report No.: LTR-AL-2022-0069

Date: July 4, 2022

Authors: Brian R. McAuliffe, Faegheh Ghorbanishohrat, and Hali Barber

Classification:	Unclassified	**Distribution:**	Limited
For:	ecoTECHNOLOGY for Vehicles Innovation Centre Transport Canada		
Project #:	A1-021114		
Submitted by:	Dr. Brian R. McAuliffe, **Senior Research Officer, Aerodynamics Laboratory**		
Approved by:	Dr. Michael Benner, **Director R&D, Aerodynamics Laboratory**		

Pages:	49	**Copy No:**	
Figures:	23	**Tables:**	13

Disclaimer

This report reflects the views of the authors only and does not reflect the views or policies of Transport Canada.

Neither Transport Canada, nor its employees, makes any warranty, express or implied, or assumes any legal liability or responsibility for the accuracy or completeness of any information contained in this report, or process described herein, and assumes no responsibility for anyone's use of the information. Transport Canada is not responsible for errors or omissions in this report and makes no representations as to the accuracy or completeness of the information.

Transport Canada does not endorse products or companies. Reference in this report to any specific commercial products, process, or service by trade name, trademark, manufacturer, or otherwise, does not constitute or imply its endorsement, recommendation, or favoring by Transport Canada and shall not be used for advertising or service endorsement purposes. Trade or company names appear in this report only because they are essential to the objectives of the report.

References and hyperlinks to external web sites do not constitute endorsement by Transport Canada of the linked web sites, or the information, products or services contained therein. Transport Canada does not exercise any editorial control over the information you may find at these locations.

Executive Summary

Emerging zero-emission heavy-duty vehicle (ZEHDV) concepts are exhibiting changes in shape from conventional heavy-duty vehicles (HDVs) that include characteristics associated with improved aerodynamic performance, including smaller front cooling-air inlets, angled wind shields and large corner radii. A project has been initiated under Transport Canada's ecoTECHNOLOGY for Vehicle program to examine the potential energy savings and range extension of ZEHDVs associated with reduced aerodynamic drag. As a first step towards demonstrating this potential, and to support regulatory-development information requests from a project stakeholder (the U.S. Environmental Protection Agency, EPA), a test campaign was undertaken in the NRC 9 m Wind Tunnel using a 30%-scale tractor-trailer model to examine the aerodynamic-drag benefits of HDVs associated with a ZEHDV shape. Three experimental tasks were carried out to examine changes to the aerodynamic drag of HDV and ZEHDV shapes for: 1) combinations of three different tractor and three different trailer configurations; 2) the addition of fender mirrors to, or the removal of main mirrors from, two tractor shapes; and 3) different flow conditions representing the wakes of various upstream-traffic conditions.

Experiments were undertaken using a 30%-scale tractor trailer model with appropriate ground-simulation conditions (spinning wheels and a moving ground plane). Three tractor models, including a day-cab shape, a sleeper-cab shape, and a zero-emission-cab shape, were each tested with three dry-van-trailer configurations with varying levels of trailer-aerodynamic technologies (no technologies, with side-skirts, and with side-skirts and a boat-tail). The zero-emission-cab shape was a first attempt at an improved shape, based on fundamental aerodynamic-shaping strategies, and was an adaptation of the day-cab model. The day-cab and zero-emission-cab tractor models were each tested with the standard main mirrors, with the addition of fender mirrors, and without any mirrors. These experiments were conducted in uniform-flow conditions with road-representative free-stream turbulence. Additionally, the zero-emission-cab model was tested in some traffic-wake scenarios representing real on-road conditions when following other vehicles, such as a compact sedan, a sport-utility vehicle, and another HDV, or when travelling in an adjacent lane to these vehicles.

Drag-coefficient and drag-area results show that changes to the shape of a day-cab tractor, based on aerodynamic considerations to represent emerging ZEHDV shapes, reduced the aerodynamic drag-area of the vehicle by 7-9%, representing about one EPA bin level (0.5 m^2). The results further show that aerodynamic improvements to the ZEHDV shape demonstrated less sensitivity to trailer configuration than did the conventional day-cab and sleeper-cab shapes. Conversely, this demonstrates that trailer-device performance was less sensitive to the ZEHDV shape than to the conventional shapes. These outcomes suggest that, with reasonable efforts to optimize the shape of HDVs based on new drivetrain/chassis architectures,

significant energy savings from aerodynamic improvements are possible over conventional North-American HDV shapes.

The main- and fender-mirror test results showed that drag reductions on the order of 4% are possible with the removal of all mirrors from an HDV tractor. Drag changes of 1-2% were documented for fender mirrors, and 3% for main mirrors. These results suggest that reducing mirror size, changing their location, or replacing mirrors with low-drag camera-based rear-view systems, can provide measurable energy savings for long-haul HDV applications.

The wake-effects testing, documented strictly for the ZEHDV model here, showed that the model experienced reduced aerodynamic drag in excess of 10% when exposed to the wakes of the specific forward-traffic conditions examined, which represent safe driving distances, even with traffic in an adjacent lane. These results provide some additional evidence that HDVs are experiencing the aerodynamic platooning effect in everyday traffic. The reduced aerodynamic drag from traffic-wake conditions suggests that current estimates of greenhouse-gas (GHG) emissions via tools like the EPA Greenhouse-gas Emission Model (GEM) may not consider the lower drag of HDVs when driving in traffic, and may therefore be overestimating GHG reductions from aerodynamic technologies/improvements via $C_D A$ values measured or assessed for isolated driving conditions.

The results presented in this report regarding the drag reduction associated with one new concept should be considered a precursory study. The findings provide a basis for next steps in examining the potential benefits of emerging ZEHDV shapes.

Contents

List of Figures

List of Tables

Nomenclature

Symbols:

A	Vehicle reference area [m^2]
C_D	Drag-force coefficient [-]
C_L	Lift-force coefficient [-]
C_P	Pitching-moment coefficient [-]
C_R	Rolling-moment coefficient [-]
C_S	Side-force coefficient [-]
C_Y	Yawing-moment coefficient [-]
ΔC_D	Drag-force coefficient difference [-]
$C_{D,W}$	Effective drag coefficient which includes resistance of wheel rotation [-]
F_D	Drag force [N]
$F_{D,W}$	Effective wheel drag force [N]
F_L	Lift force [N]
F_S	Side force [N]
ΔF_D	Change in drag force [N]
I_{WIND}	Current supplied to wheel motors subjected to wind loads [Amp]
I_0	No-load current of wheel motors [Amp]
M_P	Pitching moment [Nm]
M_R	Rolling moment [Nm]
M_Y	Yawing moment [Nm]
P	Probability-density-function for wind speed and direction [(m/s $^\circ$)$^{-1}$]
r	Wheel radius [m]
SF	Model scale factor [-]
Q	Dynamic pressure in the test section corrected for blockage [Pa]
U	Wind speed [m/s]
U_{avg}	Mean terrestrial wind speed [m/s]
U_g	Vehicle ground speed [m/s]
U_w	Terrestrial wind speed [m/s]
W	Model width [m]
WAC_D	Wind-averaged drag coefficient[-]
WAC_DA	Wind-averaged-drag-coefficient area [m^2]
ΔWAC_D	Change in wind-averaged coefficient coefficient [-]
ΔWAC_DA	Change in wind-averaged-drag-coefficient area [m^2]

X	General parameter symbol
δ	Error/uncertainty estimate of a parameter
Δ	Difference of a parameter
ν	Kinematic viscosity [m^2/s]
τ	Torque coefficient of the DC motors [Nm/Amp]
θ	Terrestrial wind angle, relative to direction of motion [°]
ψ	Wind yaw angle, relative to vehicle longitudinal axis [°]

Acronyms:

BEV	Battery electric vehicle
BLCS	Boundary Layer Control System
ECCC	Environment and Climate Change Canada
EPA	Environmental Protection Agency
FCV	Fuel cell vehicle
eTV	ecoTECHNOLOGY for Vehicles
GEM	Greenhouse-gas Emissions Model
GESS	Ground Effect Simulation System
GHG	Greenhouse Gas
HDV	Heavy-duty vehicle
LDV	Light-duty vehicle
NRC	National Research Council Canada
SATA	Subsonic Aerodynamic Testing Association
SUV	Sport-utility vehicle
V/STOL	Vertical/Short Take-Off and Landing
RTS	Road Turbulence System
RT^2S	Road Traffic & Turbulence System
ZEHDV	Zero-emission heavy-duty vehicle

1. Introduction

1.1 Background

A significant portion of the energy demand of on-road vehicles is used to overcome aerodynamic drag. For example, a typical heavy-duty tractor-trailer combination at highway speed uses approximately half of the engine power output just to overcome this air resistance (National Academy of Sciences, 2010; Patten *et al.*, 2012). As decarbonized power sources (hydrogen fuel cell vehicle - FCV, battery electric vehicle - BEV, etc.) become mature technologies and become increasingly available in a new-generation of zero-emission heavy-duty vehicles (ZEHDVs), opportunities to further improve aerodynamic performance have emerged. This arises due to the evolving drivetrain configurations and different cooling strategies that can be employed in their designs, leading to changes from conventional heavy-duty tractor shapes that require large-volume diesel engines and large flat-faced cooling-flow inlets at the front of the vehicle. Figure 1.1 shows a concept ZEHDV contrasted with a conventional HDV. These shape changes can modify the whole-of-vehicle aerodynamic performance and also lead to changes in the benefits from trailer aerodynamic technologies. Increased aerodynamic efficiency will lead to improvements in the available range from ZEHDVs, and the potential range of such vehicles will influence their penetration rates (BEVs in particular) in the long-haul market segment, as highlighted during Transport Canada's "Decarbonizing Medium- and Heavy-Duty Vehicles" engagement session in December 2021. Some ZEHDVs concepts, such as the Nikola One/Two (FCV) and Tesla Semi Truck (BEV) that exhibit some of the characteristics of the concept ZEHDV shown in Figure 1.1, are demonstrating these improved aero-

Figure 1.1: Images of a ZEHDV concept (left) and a conventional HDV (right).

dynamic strategies with tractor shapes that are much more streamlined compared to their aerodynamically-optimized diesel counterparts, while many of the established heavy-duty-vehicle (HDV) manufacturers are retaining their conventional shapes when introducing zero-emission drivetrains. Understanding the differences in aerodynamic performance of emerging ZEHDV concepts, compared to conventional shapes and drivetrains, and how they affect overall energy efficiency and range of a vehicle for different duty cycles, will inform energy-efficiency and regulatory programs aimed at transitioning the freight-transportation sector to a decarbonized future.

Transport Canada's ecoTECHNOLOGY for Vehicles (eTV) Work Plan has a two-year project on this topic, entitled *Next Generation Truck Design for Aerodynamic Efficiency and Visibility* (eTV Project B.3), with the Aerodynamic Efficiency component being led by the National Research Council Canada (NRC). Recent discussions with the US Environmental Protection Agency (EPA) and Environment and Climate Change Canada (ECCC) have identified the importance of this topic in the transition towards low-carbon and/or zero-emission transportation sectors in both Canada and the United States. Based on these early consultations, a preliminary project was initiated (named Phase 0) in March 2022 to leverage the wind-tunnel test setup of a separate project to provide an initial evaluation of emerging ZEHDV shapes and to gather additional information pertinent to EPA's next-phase greenhouse-gas-emissions regulations for HDVs. As part of the *Aerodynamics of Road Vehicles in Real-World Conditions* project (eTV Project B.1), an experiment was conducted in the NRC 9 m Wind Tunnel in February and March 2022 that used the NRC 30%-scale tractor-trailer model to examine the influence of on-road traffic conditions on the aerodynamic performance of several HDV configurations. The tractor variants of this HDV model can be adapted to represent emerging ZEHDV shapes, so an opportunity was identified to modify one of the tractor models to perform a comparison of such shapes with conventional HDV shapes. Additionally, this provided an opportunity to examine the aerodynamic-drag changes associated with different rear-view mirror combinations applied to conventional HDV and ZEHDV shapes.

1.2 Objectives

Three principal objectives were identified for the current test program:

1. Evaluate the potential for aerodynamic drag reduction from emerging ZEHDV shapes based on a preliminary modification to an existing HDV day-cab tractor model;
2. Examine the aerodynamic drag associated with main mirrors and fender mirrors on the day-cab and zero-emission-cab tractor shapes; and
3. Identify changes in aerodynamic drag of the zero-emission-cab shape associated with travelling behind other traffic at safe vehicle distances.

The experiments on which this report is based were conducted in the 9 m Wind Tunnel throughout March 2022. Chapter 2 documents the experimental setup used, with test results presented in Chapter 3. Conclusions and recommendations for next steps in the project are documents in Chapter 4.

2. Test Setup and Procedures

2.1 Test Facility

2.1.1 Background

In the early 1960s, it was found that subsonic wind tunnels in Canada were unable to accommodate vertical or short take-off and landing (V/STOL) aircraft models. V/STOL aircraft research required wind-tunnel walls, specifically the floor and ceiling, to be further away from the model than the walls of existing conventional wind tunnels. In 1963, following proposals from the aircraft industry, the National Aeronautical Research Committee recommended the construction of what is now the NRC 9 m (30 ft) Wind Tunnel. By 1969, the facility was undergoing the final stages of construction and calibration. Since its commissioning, the 9 m Wind Tunnel has been used for the study of various types of aerodynamic testing, spanning the fields of aeronautics, wind energy, wind engineering, and surface-vehicle aerodynamics. The fact that V/STOL testing requirements drove a square cross-sectional shape, as opposed to the more common horizontal rectangular shape used for conventional aeronautical testing, has also made the 9 m Wind Tunnel an ideal facility for aerodynamic testing of heavy-duty-vehicle (HDVs), since these vehicle shapes are higher than their width. The NRC Aerodynamics Laboratory is a member of the Subsonic Aerodynamic Testing Association (SATA) in good standing.

2.1.2 General Wind Tunnel Characteristics

The 9 m Wind Tunnel is a horizontal closed circuit atmospheric facility with a large test section that is suitable for testing tractor-trailer combinations up to full scale. The test section is preceded by a 6:1 contraction which transitions from a circular cross section to a filleted square cross section. The wind tunnel shell is constructed primarily of welded structural and plate steel. The circuit has a total length of 274 m, an internal duct area of 8,200 m^2, and a total volume of 47,000 m^3. The fan is powered by an air-cooled 6.7 MW DC motor that provides a maximum wind speed of approximately 55 m/s (200 km/h), or equivalently a dynamic pressure of 1850 Pa, in an empty test section. An external mechanical, pyramidal balance measures the six components of aerodynamic forces and moments. A schematic of the wind tunnel layout is provided in Figure 2.1.

The test section of the wind tunnel is surrounded by laboratory and office space, while the remainder of the circuit consists of a steel structure exposed to the outdoors. Downstream of the test section, air flows over breathers which maintain the wind-tunnel static pressure at ambient atmospheric levels. Following the breathers, the flow continues through a low-angle diffuser towards a debris screen followed immediately by the first of four 90° bends in the circuit. Over the length of the low-angle diffuser, the cross section of the wind tunnel transitions from octagonal (chamfered square) to round. The flow is guided through the bend

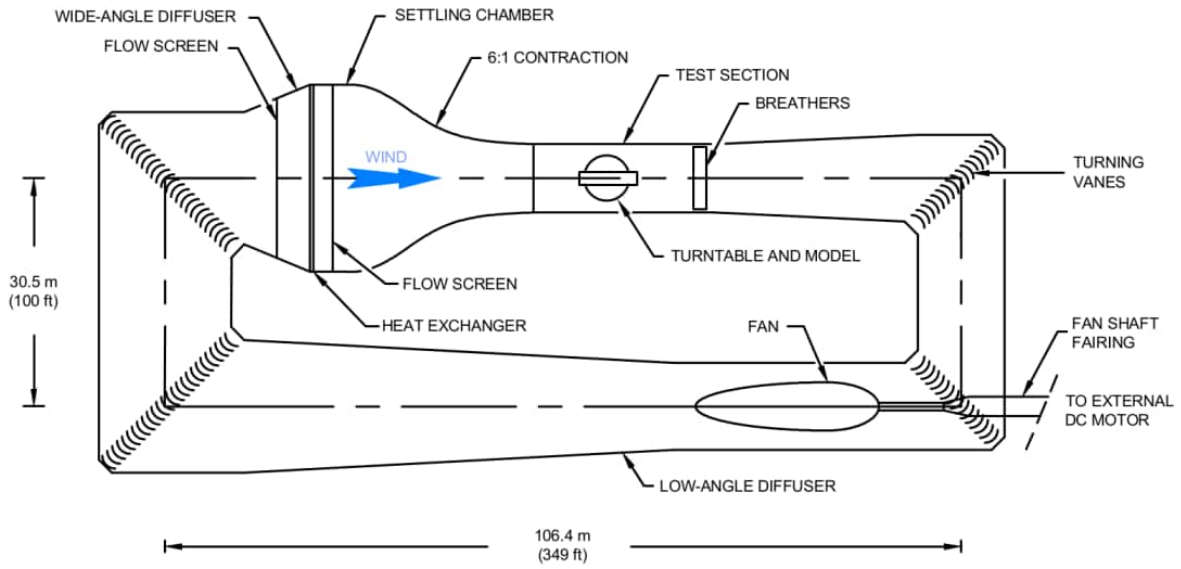

Figure 2.1: Schematic of the 9 m Wind Tunnel.

with the aid of curved steel-plate turning vanes. Turning vanes are present at all corners of the wind tunnel. At the location of the second bend in the wind tunnel, the fan shaft enters the wind tunnel shell, shrouded in a streamlined fairing. Following the second bend, the shaft enters the nose cone of the fan assembly. Following the fan, seven anti-swirl vanes straighten the flow. Downstream of the fan section, the air passes once again through a low-angle diffuser towards the third and fourth bends. After the fourth 90° bend, the air enters a wide-angle diffuser complete with wire screen for maintaining flow attachment to the wall. The wide-angle diffuser transitions into a settling chamber which houses a heat exchanger and a screen. The heat exchanger is used exclusively during warm weather to prevent the wind tunnel air and mechanical components from overheating. Following a screen which serves to increase velocity profile uniformity, the air passes through a 6:1 contraction to the test section.

2.1.3 Test Section Geometry and Configuration

A schematic of the test section is provided in Figure 2.2. The cross-sectional area of the test section is 82 m^2. From the outlet of the contraction, the walls of the test section diverge slightly (0.1 m over the 23 m length) to accommodate boundary layer growth along the walls and ceiling and prevent the development of a longitudinal static pressure gradient along the test section length. Small openings in the turntable surface allow the struts of the model to pass through to connect with the six-axis mechanical pyramidal balance.

The test-section configuration used for the current project is shown in Figure 2.3. The 30%-scale model (see Section 2.2) is mounted over the rolling-road of the Ground Effect Simulation System (see Section 2.1.4) using streamlined struts connected to the six-axis balance under the turntable floor. The Road Turbulence System (see Section 2.1.5) is faintly seen in the photograph of Figure 2.3 in the upstream settling chamber. Specific to the current tests, and seen in

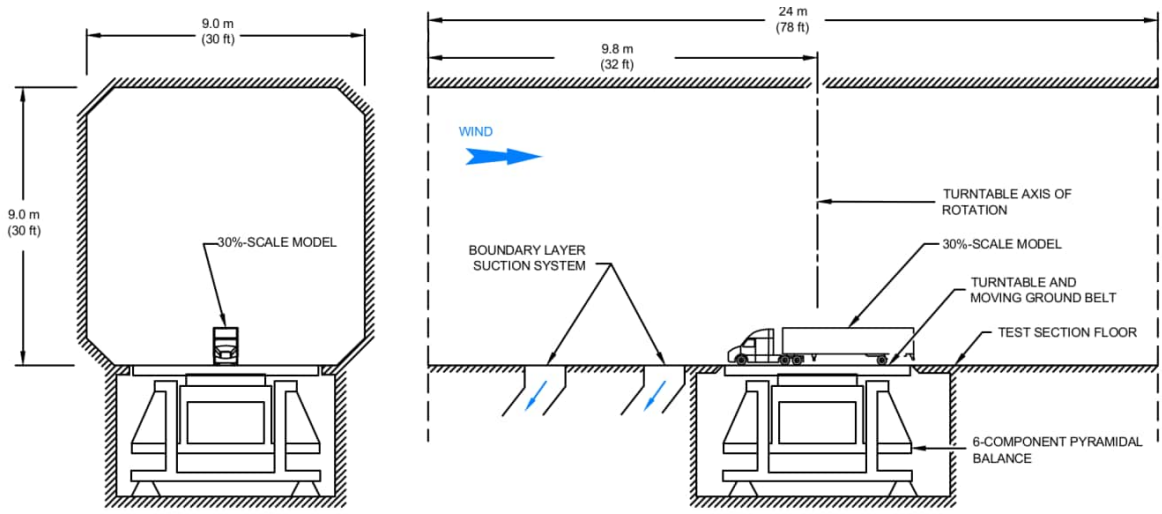

Figure 2.2: Schematic of the test section seen along the direction of wind flow (left) and from the side (right).

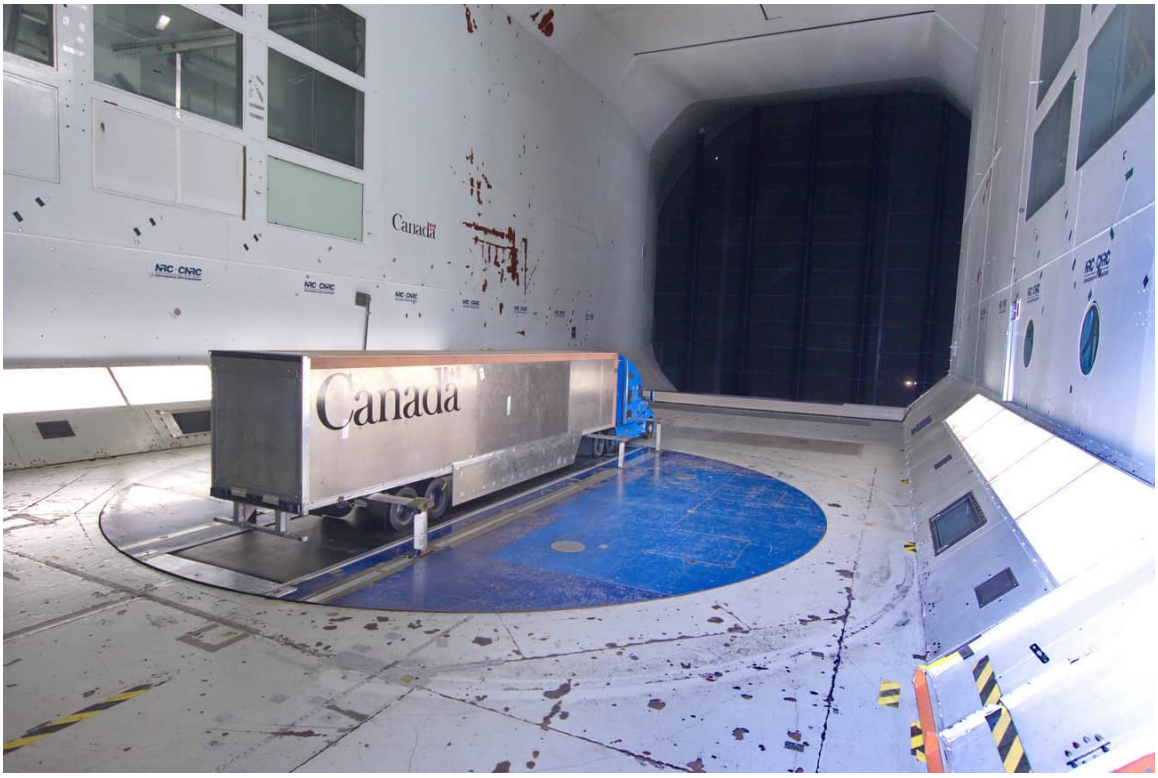

Figure 2.3: Upwind view of the test section with 30%-scale HDV model.

the photograph of Figure 2.3, is a floor-mounted assembly at the inlet of the test section that shrouds the lateral-traverse mechanisms of the wake-generator component of the Road Traffic and Turbulence System (see Section 2.1.5).

2.1.4 Ground Effect Simulation System

The 30%-scale truck model, which has spinning wheels, was designed for use with the Ground Effect Simulation System (GESS) of the 9 m Wind Tunnel that includes a boundary-layer control system (BLCS) and moving ground plane to simulate the appropriate relative motions between the vehicle, the ground, and the air. The locations of the two systems are identified in Figure 2.2 and seen in Figure 2.3). The BLCS employs two suction plenae to reduce the thickness of the floor boundary layer at the model. The displacement thickness of the boundary layer is generally 4 mm at the upwind edge of the turntable. For the current tests, that include the wake-generator-traverse assembly mounted upstream of the suction plenae, detailed boundary-layer thickness measurements were not conducted and it is unclear whether the BLCS fully removes its effects. At the model, the flow passes over either the smooth surface of 6.1 m diameter turntable, or, over the moving ground plane under and around the model. The moving ground plane, which consists of a rolling belt system, is contained within the floor turntable and therefore is always moving counter to the "direction of motion" of the truck. To avoid mechanical fouling between the wheels and the ground plane, the wheels are raised 5 mm from the surface.

The moving ground plane is 5.6 m long, yet the truck model in its test configuration is up to 6.5 m long, requiring either the forward part of the model or the back part of the model to overhang the ends of the rolling road and be suspended over the stationary floor. Model commissioning efforts used a 40 ft equivalent trailer (5.2 m length, with tractor) to examine the influence of the front, the back, or none of the model being suspended over a stationary floor. This study showed overhanging the front provided no change in drag coefficient, and overhanging the back showed a 3% increase in drag (Kirchhefer and McAuliffe, 2016). For the current testing, the model is configured as in Figure 2.3, with the front of the model suspended over a stationary floor.

2.1.5 NRC Road Traffic & Turbulence System

The NRC Road Traffic & Turbulence System (RT^2S) is comprised of two systems: the NRC Road Turbulence System (RTS), introduced in 2014; and a traffic-wake-generator system, introduced for this test campaign.

The RTS is a passive turbulence generating concept using large obstacles mounted in the settling chamber of the 9 m Wind Tunnel, observed faintly in Figure 2.3. The obstacles are removable, and installed when turbulent flow is desired. The RTS creates a model-scale terrestrial wind environment which replicates what an HDV experiences on typical North-American highways. The system provides a turbulence intensity of 4% with turbulence length-scales greater than 1 m, relative to full-scale conditions.

Truck-platooning research conducted as part of TC's eTV program has identified that vehicle wakes, the dominant source of truck-platoon fuel savings, is prevalent at safe inter-vehicle driving distances, but not to the same extent as the close-proximity platooning scenarios (McAuliffe *et al.*, 2021*a*,McAuliffe *et al.*, 2021*b*,McAuliffe *et al.*, 2021*c*). As part of the *Aerodynamics of Road Vehicles in Real World Conditions* project, conducted under the eTV program, a

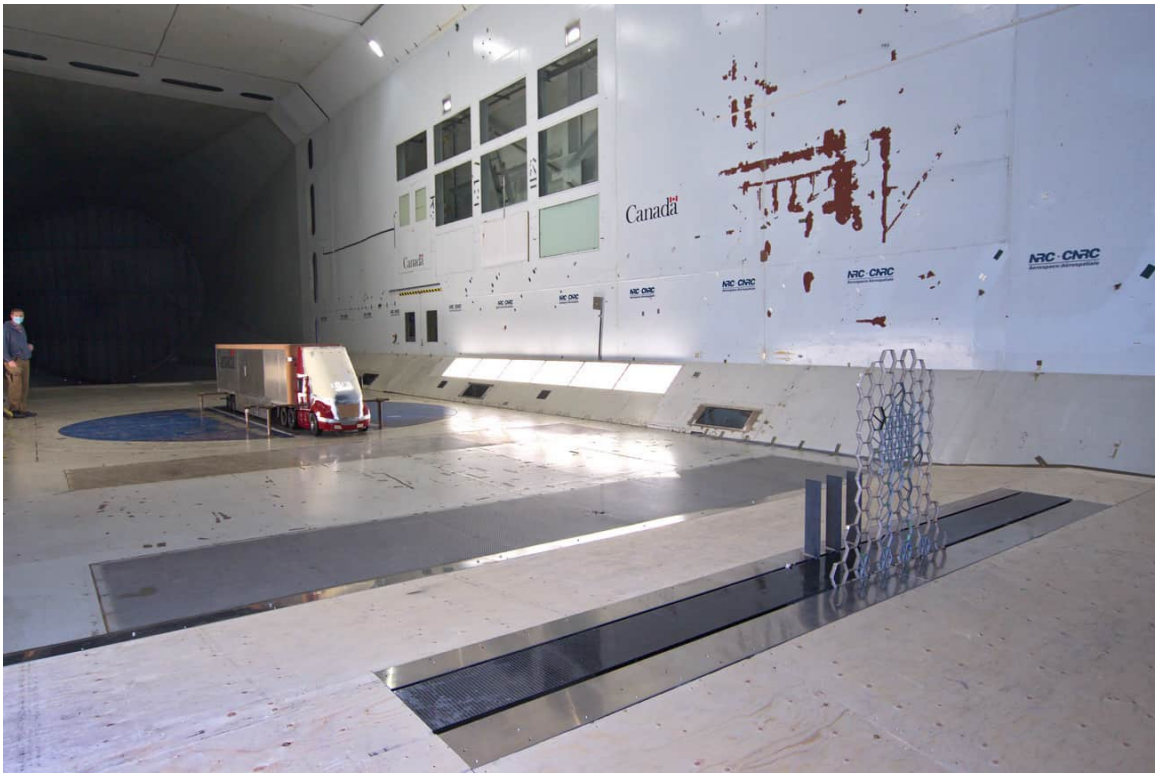

Figure 2.4: Wake-generator system, part of the NRC Road Traffic & Turbulence System, installed at the inlet of the test section (SUV-wake configuration shown).

traffic-wake-generator system was built for use with the 30%-scale truck model. The combination of the RTS and the traffic-wake-generator-system has been named the NRC Road Traffic & Turbulence System (RT^2S). Figure 2.4 shows the RT^2S installed in the 9 m Wind Tunnel with the 30%-scale truck model.

The wake-generator component of the RT^2S consists of grids and sets of up to five vertically-mounted vanes that, when combined in predefined sets of grids and vanes at specific lateral positions and vane yaw angles, creates flow patterns that represent the wakes of specific single-vehicle or traffic conditions in same- or adjacent-lane traffic conditions. Dynamic motion of the vanes are introduced, with frequency components between 1 Hz and 30 Hz, to regenerate RTS turbulence dissipated by the grids and to enhance the turbulence to represent conditions in the wakes of road vehicles. Details about the system are being documented in a separate report (McAuliffe *et al.*, 2022). The vehicle types for which wakes were simulated include:

- CAR: a compact sedan;
- SUV: a mid-sized sport-utility vehicle (SUV);
- HDV: a modern heavy-duty vehicle with sleeper-cab tractor and dry-van trailer; and
- Mixed LDV: a mix of light-duty vehicles (LDVs) including a compact sedan, a mid-sized SUV, and a large pickup truck in a two-lane arrangement.

Table 2.1: Wake-type, effective-distance, effective-lane-location, and yaw-angle (ψ) configurations of the NRC Road Traffic & Turbulence System (RT^2S) used for testing.

Vehicle Type	Vehicle Distance	Same Lane Conditions	Adjacent Lane Conditions
CAR	25 m		ψ = 4.5° ,7.5° ,11°
	50 m	ψ = -2° ,0° ,2° ,4.5°	ψ = -2° ,0° ,2° ,4.5° ,7.5°
SUV	25 m		ψ = -2° ,0° ,2° ,4.5° ,7.5° ,11°
	50 m	ψ = -2° ,0° ,2° ,4.5°	ψ = -2° ,0° ,2° ,4.5° ,7.5°
HDV	50 m	ψ = -2° ,0° ,2° ,4.5° ,7.5°	ψ = -2° ,0° ,2° ,4.5° ,7.5° ,11°
	100 m	ψ = -2° ,0° ,2° ,4.5°	ψ = -2° ,0° ,2° ,4.5°
Mixed LDV	variable	ψ = 0° ,4.5° ,7.5°	

Table 2.1 provides the specific conditions for which wakes were simulated in the current study.

2.1.6 Test Section Flow Characteristics

The maximum wind speed possible with an empty test section is 55 m/s. For testing with the 30%-scale tractor trailer combination, the maximum wind speed is 50 m/s, based on limitations of the moving ground plane. This corresponds to a Mach number of about 0.15 and a model-width-based Reynolds number of approximately 2.6 million. Due to constraints associated with the RT^2S, the test speed used for the current study was 40 m/s, corresponding to a dynamic pressure of about 1000 Pa, a Mach number of 0.12, and a Reynolds number of 2.1 million. The Mach number is below 0.25, such that considerations due to compressibility are unnecessary, and the Reynolds number is above one million, as recommended by SAE (SAE J1252, 2012).

In the vicinity of the model, the gradient of the static-pressure coefficient is small (order of 0.001 m^{-1}, Clark, 2010), and the turbulence intensity is approximately 0.5%. Cross-flow has been measured near the floor of the test section (Kirchhefer, 2017), and the model yaw angle is offset by 0.4° to align it with the flow direction. The turbulence generated by the RTS is similar to representative turbulence characteristics experienced by heavy-duty vehicles on Canadian roads, with a turbulence intensity of 4% and a turbulence length scale greater than 1 m (McAuliffe and D'Auteuil, 2016).

2.1.7 Wind Tunnel Control and Data Acquisition

The wind tunnel conditions are set by controlling the fan speed, the yaw angle of the model, the speed of the model wheels, the speed of the moving ground plane underneath the model, and the speed of the BLCS motors. Measurements of relevance to the current testing include dynamic pressure, model forces and moments, and wheel-motor current.

During testing, the operator is able to set the fan speed and the angle of the turntable. A National Instruments PXI system is used to control the fan speed and turntable position. Typ-

ically, the standard deviation of the fan speed is below 0.16 RPM, and the resolution of the model angle is 0.01°. The speed of the model wheels, moving ground plane, and BLCS motors are indirectly controlled by the set conditions of the wind tunnel (fan speed, selected blockage correction), and measured conditions (air temperature, relative humidity, absolute pressure). Automated scripts are used to define turntable angle maps for the yaw-angle conditions, and to define the lateral position, vane angle and vane-dynamic-motion profile of the RT^{2}S.

Dynamic pressure is measured at the exit of the contraction, far away from influences of the model. Measurements are made with an MKS model 698A Baratron heated, high accuracy, differential capacitance manometer. The temperature, relative humidity, and absolute static pressure of the air are measured in the settling chamber by eight RTDs, a Rotronic C94 model MP101A hygrometer, and a Paroscientific model 740-16B digital barometer respectively. Wind tunnel calibrations are used to calculate the corresponding dynamic pressure in an empty test section in real time, and standard blockage correction techniques are used to account for the increased dynamic pressure due to the presence of the model. The blockage-corrected dynamic pressure, together with the measured properties of the air, are used to calculate the wind speed in the test section. This wind speed is used to determine the appropriate speed of the moving ground plane, and the speed of the moving ground plane is in turn used to control the rotational speed of the model wheels via the supplied voltage to each motor (Maxon DC motor, RE 50, Graphite Brushes).

Force measurements are obtained from an external six-axis pyramidal mechanical balance. In the range used for the present work, the balance has a resolution of 0.4781 N in drag force, 1.209 N in side force, 1.159 N in lift force, 10.293 Nm in rolling moment, 1.795 Nm in pitching moment, and 1.958 Nm in yawing moment, and measured in the wind-tunnel coordinate system. The increments of the resolution are referred to as "balance counts." Tare values are recorded in a closed test section with still air, immediately before testing, over the range of yaw angles to be tested. New tare values are recorded after significant model changes or when the balance does not return to within three balance counts of drag or side force due to thermal effects.

2.1.8 Quality Management Certification

The NRC Aerospace Research Centre, including the Aerodynamics Laboratory, has ISO 9001 certification. All critical instrumentation is calibrated following appropriate calibration schedules, and all calibrations are documented and traceable. Facility validations and verifications are performed as part of the certified quality management process.

2.2 Test Models

Testing was undertaken with the NRC 30%-scale tractor-trailer model. This is a detailed wind-tunnel model of a heavy duty vehicle (HDV), capable of adopting a range of configurations typical of full-scale HDVs on North American roads. The model can accommodate different gap sizes, cab styles, trailer types, and wheel sizes.

Three variants of the tractor model were tested in the current study. Underbody structures (fuel tanks, exhaust-system components, mud flaps, etc.) are present with high fidelity in all three versions. The three tractor variants, all of which have a 6x4 axle arrangement, are:

- Day-cab tractor (Figure 2.5): The initial version of this tractor was modelled after an International/Navistar ProStar short sleeper cab with modifications made to the bumper, hood, A-pillars and roof fairing per Navistar's request. The short-sleeper configuration was designed to convert to a smaller high-roof day-cab variant, which uses the same components from the driver cab forward, with a different cab-back component and a different high-roof fairing designed by NRC to smoothly guide the flow onto the trailer.
- Long-sleeper-cab tractor (Figure 2.6): This newest version of the tractor is based on a 3D scan of a model-year 2016 Kenworth T680 high-roof long-sleeper cab that was loaned by ECCC (VIN 1XKYDP9X9HJ989040). This model represents, to the best of the designers capabilities, the exact external shape of the full-scale vehicle. The wheelbase-adjustable chassis from the short-sleeper model was used as the underlying structure for this model, therefore the engine-bay, suspension, and drive-line components differ somewhat from the scanned vehicle.
- Zero-emission-cab tractor (Figure 2.7): The adapted-ProStar day-cab tractor was modified to fill in the region above the hood and forward of the windscreen to provide a shallower surface angle and large corner radii, similar to characteristics found on emerging ZEHDV shapes like the Tesla Semi and the Nikola One. The modification, which is a hand-carved modelling-foam insert, is shown at its various stages of fabrication in the lower images of Figure 2.7. The shape was based, in part, on a research model developed at NRC for an earlier eTV project that contained shape characteristics of emerging ZEHDV concepts (documented by McAuliffe and D'Auteuil, 2016). To simulate the reduced cooling air-flow requirements for ZEHDVs, the large upper front grille was covered, while the lower opening in the bumper remained open.

The tractor model chassis, on which all model variants are based, has an engine bay with a representative static engine and its auxiliary components, and uses porous screens to simulate the cooling system for an appropriate level of cooling air flow through the cooling system and engine bay. The model has an electric-wheel-drive system with treaded-wheel models. The tractor-trailer gap was set to 0.343 m (1.14 m / 45 in full scale) for the current tests.

The 30%-scale trailer model represents a 53 ft box-van with a tandem-axle wheel setup, and also has an electric-wheel-drive system and treaded-wheel models. Figure 2.8 shows the trailer bogie and wheel details. The rear trailer axle is positioned 0.91 m from the trailer rear surface (3.05 m full scale). The trailer is modelled after a combination of Wabash and Manac trailers. The standard setup represents a dry-van trailer. The trailer model has many details of a real trailer, including the landing gear, under-body ribs, a rear-impact guard, a drip rail along the upper edges, a rain gutter at the top aft edge, and light- and door-hardware details. Three variants of the trailer model were used for testing, with different drag-reduction technologies installed. Figure 2.9 shows the standard trailer model, without any drag-reduction technologies, while Figure 2.10 shows the trailer model outfitted with side-skirts and a boat-tail. A configuration with only side-skirts was also tested. For ease of model changes, a simpler back plate was used on the trailer model that does not include door hardware or hinges. This plate

Figure 2.5: Tractor-trailer model with day-cab tractor. Top: Model overview. Bottom: Underbody details (short-sleeper-cab variant shown on jacks, without wheels).

Figure 2.6: Tractor-trailer model with sleeper-cab tractor. Top: Model overview. Bottom: Underbody details.

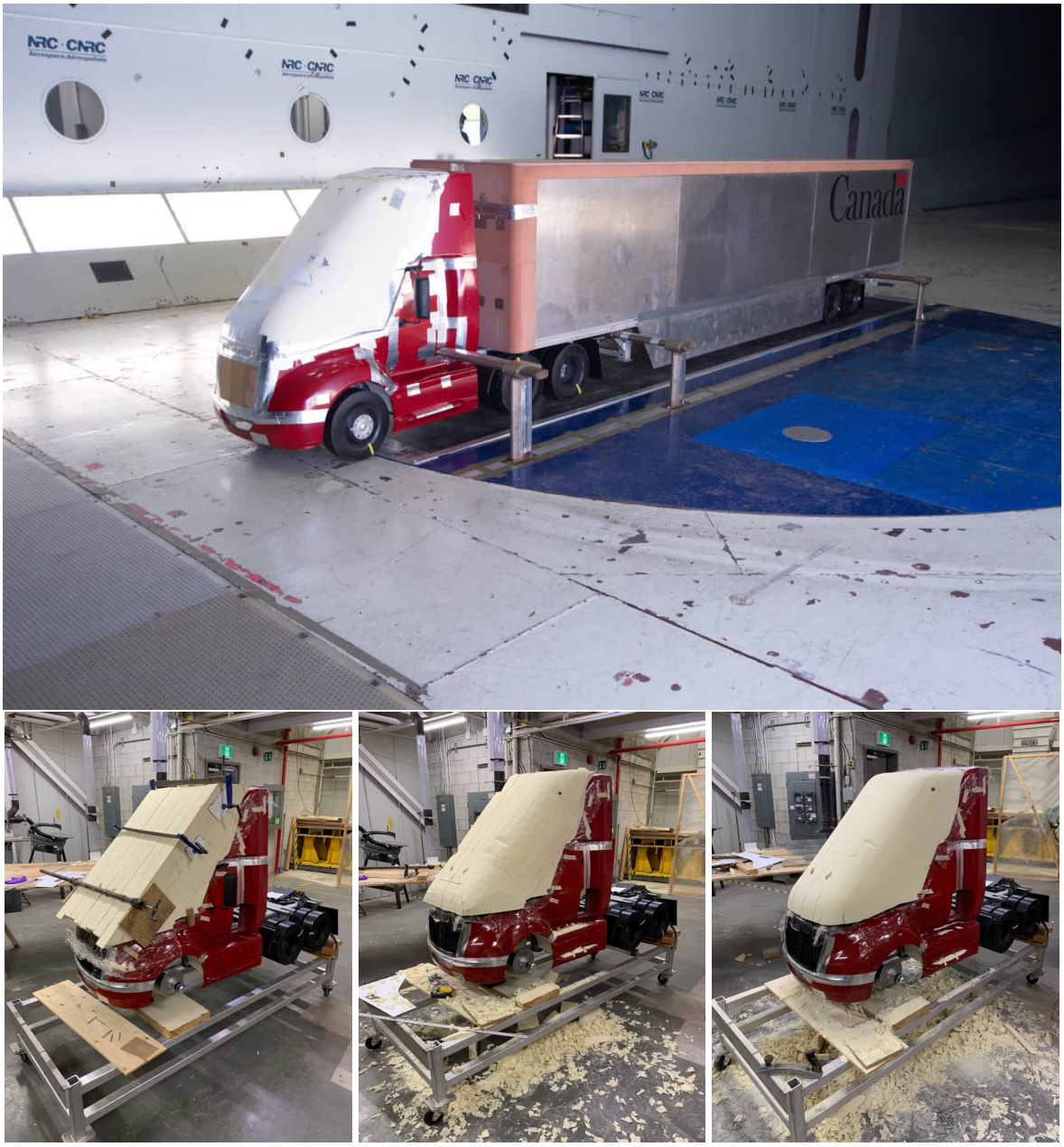

Figure 2.7: Tractor-trailer model with zero-emission-cab tractor. Top: Model overview. Bottom: Stages of modification (glued-block installation, initial hand-carved block, final smoothed block).

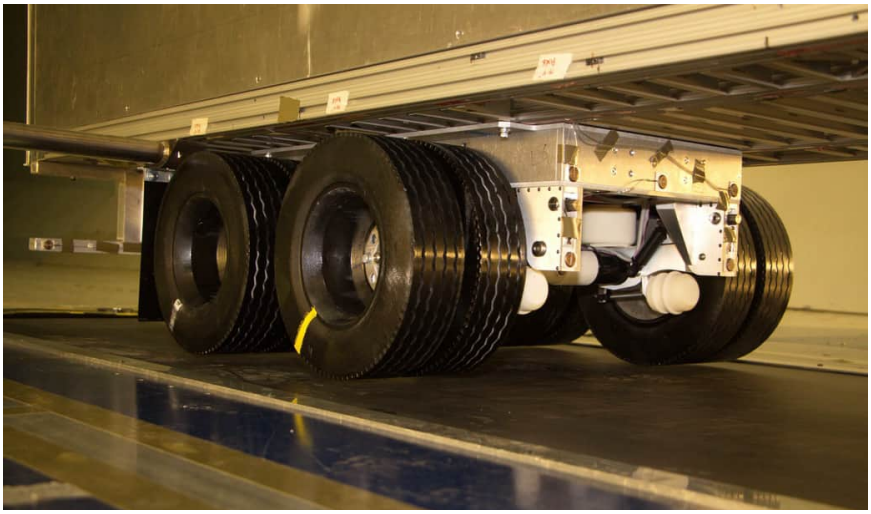

Figure 2.8: Trailer bogie and wheel assemblies.

is the standard plate used when installing boat-tail model. To save model-change time and maximize the testing undertaken within the project budget, this simpler plate remained on the model for all tests. Early commissioning tests with the full-detailed back plate, in 2016, did not show any measurable difference from a flat back with no details, and therefore the use of the simpler plate was not expected to influence the test results.

The side-skirt and boat-tail models were designed by NRC and used in previous test programs (McAuliffe and Wall, 2016; McTavish and McAuliffe, 2021). The side-skirt model represent flush-mounted skirts with full-scale dimensions of 7.9 m length (26 ft) and 0.91 m height (3 ft), with a chamfered front edge. The boat-tail model is a three-panel concept with full-scale dimensions including a 0.91 m (3 ft) maximum extension at the top, 11° top-panel inset angle, 13% side-panel inset angle, and a top-panel offset from the roof of 0.033 m (1.3 in).

Two sets of mirror models were used during testing to examine the aerodynamic drag associated with mirrors on HDVs, and are shown mounted to the cay-cab and zero-emission-cab model in Figure 2.11. The door-mounted main mirrors are based on the design associated with the ProStar tractor model, typically referred to as "west-coast" mirrors, representing the type used on these tractors until the mid 2010's. Fender-mirror models were designed and built for an unpublished NRC test campaign in 2016, representing the style of fender mirrors used on Volvo VNL tractors at that time.

Test-article descriptions are provided in Table 2.2 for the tractor models and Table 2.3 for the trailer model. All dimensions relevant to the test (per SAE J1252, 2012) are shown in Figure 2.12 and listed in Table 2.4.

The model is supported by six streamlined struts. The six struts extend horizontally from the model: four from the lower edge of the trailer and two from the tractor. All struts connect to vertical streamlined columns which are connected to a balance underneath the wind-tunnel floor. The support struts and internal structure of the model are sufficiently rigid not to deflect significantly under wind loads. The model wheels are suspended above the belt/floor surface

Figure 2.9: Standard-trailer model.

Figure 2.10: Trailer model with side-skirts and boat-tail.

Figure 2.11: Main-mirror and fender-mirror model mounted to the day-cab (left) and zero-emission-cab (right) tractor models. Top row - both sets of mirror models installed. Bottom row - no mirror models installed.

with a maximum clearance of 5 mm. For all but the front tractor wheels, the model wheels are above a moving ground plane.

Table 2.2: Test-article description - tractor models.

Day-cab tractor characteristics	
Manufacturer and model	adaptation of International ProStar Short-sleeper-cab (modified bumper, hood, A-pillar, roof fairing)
Year	characteristic of 2006-2017 model years
Wheelbase	3.87 m (full-scale)
Tire size	295/75R22.5 on all three axles
Number of axles	3 (6x4 configuration)
Suspension type	leaf-spring on steer axle, air-ride on drive axles
Cab type size	high-roof day-cab
Roof fairing type	full-height aerodynamic fairing
Tractor-to-trailer gap	45 inch (full-scale) back of cab to front of trailer (28 inch aero gap, accounting for 17 inch side extenders)
Mud flap location	located behind aft drive wheels
Mud flap type	flexible non-porous (represents rubber mud-flaps)

Long-sleeper-cab tractor characteristics	
Manufacturer and model	Kenworth T680 (VIN 1XKYDP9X9HJ989040)
Year	2016
Wheelbase	5.32 m (full-scale)
Tire size	295/75R22.5 on all three axles
Number of axles	3 (6x4 configuration)
Suspension type	leaf-spring on steer axle, air-ride on drive axles
Sleeper type size	76-inch high-roof sleeper
Roof fairing type	full-height aerodynamic fairing
Fuel tank sizes	approx. 90 gal
Fuel tank position	mounted to frame rails, covered by tractor side-skirts
Tractor-to-trailer gap	45 inch (full-scale) back of cab to front of trailer (23 inch aero gap, accounting for 22 inch side extenders)
Mud flap location	located behind aft drive wheels
Mud flap type	flexible non-porous (represents rubber mud-flaps)

Table 2.3: Test-article description - trailer model.

Trailer characteristics	
Trailer manufacturer	features form Wabash and Manac trailers
Trailer type	dry-van
Trailer axle configuration	tandem
Trailer model year	representative of 2010+ models
Trailer model name	N/A
Trailer length	636 inch, 16.15 m (4.854 m model scale)
Trailer height	box is 118 inch, 2.99 m (0.899 m model scale) total is 162 inch, 4.11 m (1.234 m model scale)
Trailer width	102 inch, 2.6 m (0.78 m model scale)
Bogey position	rear of trailer to center of tandem axle 144 inch, 3.66 m (1.097 m model scale)
Front corner radius	6 inch, 0.152 m (0.046 m model scale)
Tire size	295/75R22.5 on all axles
Mud flap location	trailer-underside mounted, located behind aft bogie axle
Mud flap type	flexible non-porous (represents rubber mud-flaps)
Refrigeration unit (optional)	similar size and shape to commercial units
Fuel tank (optional)	mounted aft of landing gear

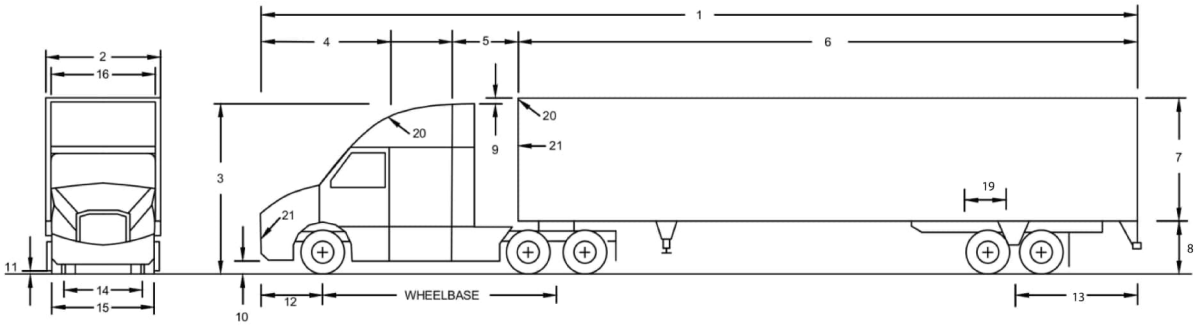

Figure 2.12: NRC 30%-scale tractor-trailer model - locations of relevant dimensions (SAE J1252). Dimensions are listed in Table 2.4.

Table 2.4: Dimensions of the 30%-scale tractor-trailer models. Dimensions are indicated in Figure 2.12. Dimensions applicable to all tractor and trailer configurations unless otherwise indicated. Note that dimensions 17 and 18 are not listed in the table as they are indicated as obsolete in SAE J1252.

Characteristic	Dimension (FS - Full-scale Value)
1. Overall length	6.614 m (22.05 m FS)† / 6.110 m (20.37 m FS)‡
2. Overall width	0.78 m (2.6 m FS)
3. Overall front height	1.193 m (3.98 m FS)† / 1.220 m (4.07 m FS)‡
4. Cab/sleeper length	1.418 m (4.73 m FS)† / 0.924 m (3.08 m FS)‡
5. Gap length	0.343 m (1.14 m FS)
6. Trailer/box length	4.852 m (16.17 m)
7. Rear body height	0.899 m (2.99 m FS)
8. Rear Ground Clearance	0.335 m (1.12 m FS)
9. Roof height differential	0.041 m (0.14 m FS)† / 0.014 m (0.05 m FS)‡
10. Front ground clearance	0.078 m (0.26 m FS)† / 0.085 m (0.28 m FS)‡
11. Minimum ground clearance	0.05 m (0.167 m FS), at rear transfer casing
12. Front overhang	0.393 m (1.31 m FS)† / 0.379 m (1.263 m FS)‡
13. Rear overhang	1.094 m (3.64 m FS)
14. Front track width	0.637 m (2.12 m FS)
15. Front bumper width	0.724 m (2.41 m FS)† / 0.709 m (2.36 m FS)‡
16. Roof width	0.705 m (2.35 m FS)† / 0.719 m (2.40 m FS)‡
19. Wheel diameter	0.305 m (1.02 m FS)
20. Leading edge geometry	tractor - curved, trailer - square edge
21. Front side edge geometry	tractor - curved, trailer - 0.046 m radius (0.15 m FS)
22. Wheelbase	1.643 m (5.48 m FS)† / 1.161 m (3.87 m FS)‡
23. Frontal area (reference area)	0.962 m^2 (10.7 m^2 FS)

† specific to long-sleeper-cab tractor setup
‡ specific to day-cab tractor setup

2.3 Test Procedure

Testing was conducted in accordance with SAE recommended practices (SAE J1252, 2012), EPA modifications thereof (noted in §1037.526 and §1037.530 of U.S. EPA and U.S. DOT, 2016), and supplemented by NRC best practices for ground-vehicle wind-tunnel testing. Measurements were taken over a duration of sufficient time (30 seconds) such that the random uncertainties in average values are small compared to the bias uncertainties of the instruments. The standard yaw-sweep used for uniform-flow testing was: +4.5°, -15.0°, -11.0°, -7.5 °, -4.5°, -2.0°, 0°, +2.0 °, +4.5°, +7.5 °, +11.0°, +15.0°, -4.5°. Comparing measurement results from the repeat values at yaw angles of -4.5°and +4.5°provided a data quality check at the end of each test run. Occasionally, specific test configurations were repeated throughout the test program for longer-term-repeatability checks and uncertainty quantification. The yaw angles were selected based on NRC's standard research yaw sweep (0°, ±1.5°, ±4.5°, ±7.5°, ±11.0°, ±15.0°) with the ±1.5° conditions exchanged for ±2.0° to provide improved resolution of C_D-vs-yaw gradients associated with wake-effects testing with the RT^{2}S.

2.4 Data Reduction

The parameter of most interest for the current study is the drag coefficient, defined as

$$C_D = \frac{F_D}{Q\ A} \tag{2.1}$$

where F_D is the measured drag force in vehicle-oriented coordinates, Q is the dynamic pressure, and A is the vehicle reference area (taken here as vehicle height × vehicle width). Although not discussed explicitly in this report, data for the other force and moment coefficients are provided in an appendix. Those other coefficients are defined as:

$$\text{Side-force coefficient} \qquad C_S = \frac{F_S}{Q\ A} \tag{2.2}$$

$$\text{Lift-force coefficient} \qquad C_L = \frac{F_L}{Q\ A} \tag{2.3}$$

$$\text{Rolling-moment coefficient} \qquad C_R = \frac{M_R}{Q\ A\ W} \tag{2.4}$$

$$\text{Pitching-moment coefficient} \qquad C_P = \frac{M_P}{Q\ A\ W} \tag{2.5}$$

$$\text{Yawing-moment coefficient} \qquad C_Y = \frac{M_Y}{Q\ A\ W} \tag{2.6}$$

Regulatory protocols use drag area ($C_D A$) as the metric of interest, based on the full scale of the vehicle. The drag area is calculated as

$$C_D A = \frac{F_D}{Q\ SF^2} \tag{2.7}$$

where SF is the scale factor (0.3 in this case). Drag area has units of m^2. Although it has units of area, Equation 2.7 demonstrates that no area measurement is required for its calculation.

However, for ease of scaling results presented in this report, the reader may use the full-scale reference area, which is 10.66 m^2 for the current study.

The wind-tunnel data provide wind speed, properties of the air, wheel power, and aerodynamic force and moment data in the coordinate system of the wind tunnel. From the acquired wind-tunnel data, and after conversion from acquired values to appropriate SI units, the process of data reduction consists of:

1. Calculating the reference dynamic pressure and static pressure in the test section based on the wind tunnel calibration;
2. Calculating the flow parameters in the test section (air properties and wind speed) using standard fluid dynamics equations;
3. Calculating the force and moment coefficients at the balance resolution centre;
4. Translating the moment coefficients to the reference location (front of trailer model, laterally centred, at the floor);
5. Calculating and applying wall corrections to the flow parameters and to the force and moment coefficients, correcting the force and moment coefficients to account for wind tunnel blockage, and correcting the yaw angle for wall interference;
6. Transforming force and moment coefficients from a wind-tunnel coordinate system to a model axis coordinate system;
7. Calculating the aerodynamic torque from all wheel motors, formulating an effective model-axis force coefficient, correcting for blockage, and adding it to the model-axis drag coefficient;
8. Applying strut-tare and interference corrections to the force and moment coefficients, appropriately accounting for the blockage corrections and for the influence of wakes;
9. Performing calculations and corrections for other measurements such as surface pressures and front-grille anemometers; and
10. Calculating an estimate of the wind-averaged-drag-coefficient area, WAC_DA, according to Section 2.4.4.

The following sections provide an overview of some of the above steps.

2.4.1 Wall Interference Corrections

To account for confinement of the flow within the closed-wall test section, wall-interference corrections are applied. The Thom-Heriot blockage-correction method (SAE SP-1176, 1996) is applied for HDV testing in the 9 m Wind Tunnel. The method makes use of model and test-section geometry, and the model force coefficients, to determine a dynamic pressure correction and wake-drag-increment correction that are appropriately applied to the force and moment coefficients. At non-zero-yaw conditions, the interaction of the model side force on the flow and the presence of the test section walls influence the flow-field around the model in a manner

equivalent to increasing the relative wind/yaw angle. This is corrected using standard wind-tunnel methods (Barlow *et al.*, 1999).

2.4.2 Strut Influence Corrections

The six model mounting struts are not shielded from the wind and therefore any wind-loads measurements contain a component associated with the strut, called the strut-tare loads. The strut-tare drag loads are on the order of 5% of the model drag, necessitating correction of the measured data. Characterization of the wind loads experienced by the struts (strut tare loads) and their interference effects on the model wind loads (strut interference loads) was performed during commissioning efforts of the various models.

Measurements of the strut wind loads were performed in a configuration in which the struts were connected to the balance and the model was supported rigidly to the test section floor without contacting the struts. Strut-tare loads were recorded over a large range of model yaw angles ($\pm 15^{\circ}$), and converted to coefficient form.

The presence of the struts also influence the wind patterns and the wind loads experienced by the model, but to a lesser extent than the strut tare loads (1-2%). These strut interference loads were measured with the truck model mounted to the balance through posts in the floor (GESS not installed during these tests), with and without the struts located in their respective locations on the wind-tunnel floor.

For wake-effects testing with the RT^{2}S, the strut-tare and interference corrections are expected to be influenced by the reduced wind speeds in the wake. McAuliffe *et al.* (2022) describe the manner in which these corrections are adapted for wake-effects testing.

2.4.3 Aerodynamic Resistance of the Wheels

The overall aerodynamic resistance to the motion of a ground vehicle includes the drag force acting on the vehicle, in-line with the direction of motion, as well as the aerodynamic torque experienced by the wheels. The engine must generate sufficient power to counter both aerodynamic resistances, and hence, both aerodynamic resistances play a role in fuel consumption. To incorporate aerodynamic torque in the calculation of a drag coefficient, wheel torque is converted to an effective drag force acting on the model, converted to coefficient form, and added to the "in-line" drag coefficient, C_D. The resulting drag coefficient, which includes the contribution of wheel resistance, and the effective drag force are

$$C_{D,W} = C_D + \frac{F_{D,W}}{QA} \tag{2.8}$$

where

$$F_{D_W} = \sum \frac{(I_{WIND} - I_0)\tau}{r} \tag{2.9}$$

and where $F_{D,W}$ is the effective drag due to the wheels, calculated as the sum of effective drag contributions from each wheel. I_{WIND} is the current supplied to the motor during testing, I_0 is

a no-load current removed as a tare, τ is the torque coefficient of the motor and r is the radius of the wheel.

Once converted to a force coefficient, the effective wheel-torque drag is on the order of 3-4% of the model drag.

2.4.4 Wind-Averaged Drag Coefficient

To provide a single representative measure of the aerodynamic performance of a ground vehicle with which different configurations can be compared, a wind-averaged-drag coefficient (WAC_D) can be defined for a given ground speed (U_g). The approximation for WAC_D defined by SAE J1252 (2012) makes use of the distribution of C_D with yaw angle, combined with a single mean terrestrial wind speed (U_{avg}) that represents long-term averaged conditions experienced across the United States weighted by the annual truck distance travelled in each state SAE J1252 (2012). Recent regulatory procedures by the EPA have simplified the quantification of wind averaging by recognizing a correlation between SAE-method results for 65 mph ground speed and the drag coefficient or drag-area calculated as an averaged of values measured at yaw angles of $\pm 4.5^\circ$ (U.S. EPA and U.S. DOT, 2016). Some recent work by the authors has identified quantifiable differences associated with the SAE approach (named here the "Mean-wind" method) and the EPA approach (named here the "2-point" method) as compared to the general form of the WAC_D definition (named here the "Full-wind" method), specifically for cases with significant asymmetries of C_D with yaw angle which are observed from wake-effects testing. Differences in WAC_D between the methods of up to 0.011 for the mean-wind method and up to 0.017 for the 2-point method, relative to the Full-wind method, have been observed for results in the current data set, which is on the order of 2% and 3% of the model wind-averaged-drag coefficient. These differences are documented in Appendix B. For various reasons, including needs of the EPA and reference to other studies, wind-averaged values calculated using the three methods are presented in this report. The following describes the calculation procedures for the three methods, with reference to Figure 2.13.

Full-wind Method

The procedure to calculate WAC_D involves averaging the drag due to the vector combination of the ground speed with all wind-speed and yaw-angle combinations based on a prescribed

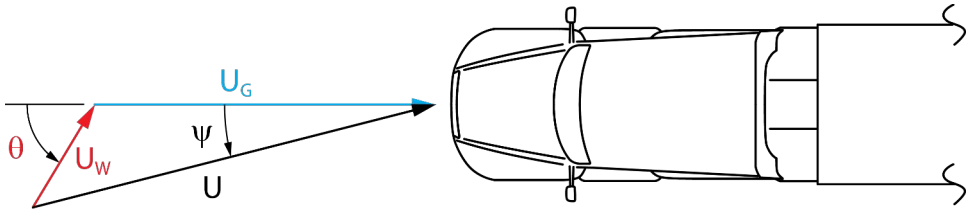

Figure 2.13: Vector combination of the terrestrial wind vector (U_w) and the vehicle motion vector (U_g) to define the relative wind vector (U).

distribution of terrestrial wind speeds and directions. The equation for the wind-averaged-drag coefficient is:

$$WAC_D(U_g) = \int_0^{2\pi} \int_0^{U_{w,max}} C_{D,W}(\psi) \left(\frac{U}{U_g}\right)^2 P\left(U_w, \theta\right) d\theta dU_w \tag{2.10}$$

where θ is the terrestrial wind angle and the resultant wind-speed ratio is

$$\left(\frac{U}{U_g}\right)^2 = 1 + \left(\frac{U_w}{U_g}\right)^2 + 2\left(\frac{U_w}{U_g}\right)\cos\theta \tag{2.11}$$

and where the yaw-angle of the wind relative to the direction of motion is

$$\psi = \tan^{-1}\left[\frac{(U_w/U_g)\sin\theta}{1 + (U_w/U_g)\cos\theta}\right] \tag{2.12}$$

A probability-density-function for wind speed and direction, $P(U_w, \theta)$, has been selected based on the U.S. wind-climate data defined by Buckley *et al.* (1978), for which its mean wind speed of 7 mph (11 km/h) was re-confirmed in 2012 by SAE (SAE J1252, 2012), providing justification for using this distribution. The data of Buckley *et al.* is shown in Figure 2.14 along with a best-fit Weibull distribution function that has been used with a numerical integration scheme to solve Equation 2.10 for all data sets presented in the current paper. The WAC_D values presented in this paper represent those calculated for the wind-distribution of Figure 2.14 and a vehicle ground speed of U_g = 105 km/h (65 mph). Note that the calculation of WAC_D uses the effective drag coefficient $C_{D,W}$, which includes the aerodynamic resistance to wheel rotation.

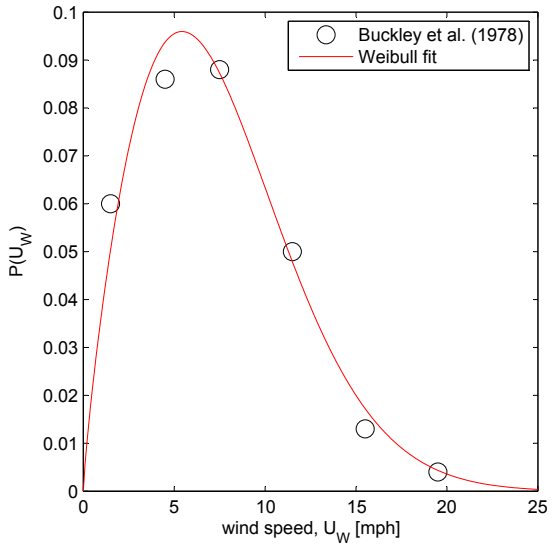

Figure 2.14: Wind distribution used for the current study, based on data presented by Buckley et al. (1978).

Mean-wind Method

For the Mean-wind method, defined by SAE (SAE J1252, 2012), the wind-averaged drag coefficient, WAC_D, for ground speed U_g, is based on Equation 2.10 with the probability distribution replaced with the mean wind speed. This approach assumes an equal probability of this "constant" mean wind speed from any direction, such that Equation 2.10 reduces to:

$$WAC_D(U_g) = \frac{1}{2\pi}\int_0^{2\pi} C_{D,W}(\psi)\left[1+\left(\frac{U_{avg}}{U_g}\right)^2+2\left(\frac{U_{avg}}{U_g}\right)\cos\theta\right]d\theta \tag{2.13}$$

where

$$\psi = \tan^{-1}\left[\frac{(U_{avg}/U_g)\sin\theta}{1+(U_{avg}/U_g)\cos\theta}\right] \tag{2.14}$$

in which U_{avg} is the mean terrestrial wind speed, set as 11 km/h or 7 mph (SAE J1252, 2012).

2-point Method

EPA GHG regulations (U.S. EPA and U.S. DOT, 2016) require a simplified method for evaluating the wind-averaged drag that differs from the SAE-defined mean-wind formulation that had been previously used for the EPA SmartWay program (EPA, 2015). In lieu of acquiring data over a large range of yaw angles from which the wind-averaged-drag coefficient is evaluated, the EPA procedure assumes that the drag-coefficient at 4.5°yaw angle is a representative measure, and therefore requires an average of the drag-coefficient at -4.5°and +4.5°as a representation of the wind-averaged drag coefficient. The four corresponding data points within each test run are therefore averaged to provide this representation:

$$WAC_D = \frac{1}{N_{\pm 4.5^o}}\sum C_{D,W,\pm 4.5^o} \tag{2.15}$$

where $N_{\pm 4.5^o}$ is the number of individual values used in the averaging process.

2.4.5 Uncertainty Requirements and Calculation

Any calculated change (Δ) in wind-averaged drag coefficient or drag area is associated with an uncertainty (δ), such that the measured value is in the interval $\Delta WAC_D \pm \delta\Delta WAC_D$ or $\Delta WAC_D A \pm \delta\Delta WAC_D A$.

The uncertainty analysis undertaken here is based on the procedures established in Appendix B of the SAE recommended practice for wind-tunnel testing of trucks and buses (SAE J1252, 2012), with an adaptation for calculating the uncertainty of the ΔC_D and ΔWAC_D values associated changes to the test models. References to SAE J1252 are for version JUL2012. In the following discussion, the terms systematic-error (used in J1252) and bias-error (used here) are synonymous. Uncertainty calculations are performed with C_D values, as opposed to $C_D A$

values, for consistency with J1252 procedures, with re-scaling of the uncertainties to their respective $C_D A$ units for the final documentation.

For individual δC_D values the random-error estimation of Section B.2 (of J1252), the bias-error estimation of Section B.3 (of J1252), and the combined expanded uncertainty of Section B.4 (of J1252) are applied as defined in SAE J1252 version JUL2012.

The methods defined in SAE J1252 do not provide a formal procedure for calculating $\delta\Delta C_D$ or $\delta\Delta C_D$ values. As such, the calculation of the combined expanded uncertainty based on individual δC_D estimates (Section B.4 of J1252) is often used for lack of an appropriate approach. This uses the uncertainty values from each respective test configuration to be compared and calculates a further combined-expended-uncertainty result by compounding all uncertainty values under an assumption that each is fully independent of each other. Although this approach does provide an uncertainty interval for the device-performance value, the calculated interval is generally much larger than would be achieved with procedures defined for differences (ΔC_D) as opposed to absolute (C_D) measurements, and is therefore a conservative estimate. This method does not account for the component of the bias uncertainty that remains the same (magnitude and sign) in each measurement. These elemental uncertainty components are not independent and their compounding is what leads to larger uncertainty estimates than what are truly represented by the various uncertainty sources. These components of the bias uncertainty are considered correlated between each calculated result, such that when subtracting two results for a Δ value, these uncertainties can cancel rather than compound. This can be demonstrated by the following example:

> Take, for example, a measurement system for which the only error is an unknown offset (δ) that remains constant, regardless of the state of the system. Two states X_1 and X_2 are then measured, and the final result of each respective state must contain the offset uncertainty as $X_1 + \delta$ and $X_2 + \delta$. If the difference between these values is desired, the following result is found:
>
> $$\Delta X = (X_2 + \delta) - (X_1 + \delta) = X_2 - X_1 \tag{2.16}$$
>
> which has no error component because the constant magnitude and sign of δ is cancelled through the subtraction process. The use of a combined-expanded-uncertainty approach would lead to
>
> $$\Delta X = (X_2 \pm \delta) - (X_1 \pm \delta) = (X_2 - X_1) \pm \sqrt{2}\delta \tag{2.17}$$
>
> which is inappropriate for this type of error and leads to an overestimate of the uncertainty.

For the 30%-scale HDV testing in the NRC 9 m Wind Tunnel, many error sources are independent between two calculated C_D values, but some are correlated and should be adequately accounted for in the uncertainty analysis. Consider the following equation which represents the change in drag coefficient between two test configurations:

$$\Delta C_D = \frac{F_{D,2}}{QA} - \frac{F_{D,1}}{QA} \tag{2.18}$$

Assuming that the drag values for the two configurations ($F_{D,1}$ and $F_{D,2}$) were acquired at the same dynamic pressure (Q), Equation 2.18 reduces to the following form (since A is un-

changed):

$$\Delta C_D \approx \frac{\Delta F_D}{QA} \tag{2.19}$$

The elemental bias uncertainty of this equation, calculated using a Taylor Series expansion in the same manner as Equation B8 in J1252, is:

$$\delta^2_{\Delta C_D} = \left[\frac{1}{QA}\delta_{\Delta D}\right]^2 + \left[\frac{-\Delta F_D}{Q^2 A}\delta_Q\right]^2 \tag{2.20}$$

Since Equation 2.20 represents bias uncertainties only and is defined based on a difference between two test runs/configurations, the $\delta_{\Delta F_D}$ and δ_Q terms can therefore be represented as uncertainties associated with ΔF_D and ΔQ between the two test runs/configurations as opposed to the full magnitudes of F_D and Q. The manner in which each are treated are as follows:

- $\delta_{\Delta F_D}$ based on ΔD: Uncertainties associated with the balance measurements of the NRC 9 m Wind Tunnel have been defined as constant between any two measurements (ΔF_D), whether they be individual-run measurements (wind-on minus wind-off values) or differences from run to run (wind-on run 2 minus wind-on run 1), and therefore the first term of Equation 5 is treated the same as with the individual-C_D values, using the same $\delta_{\Delta D}$ value of 1.4 N (95% confidence value).
- δ_Q based on ΔQ: Operational procedures in the NRC 9 m Wind Tunnel ensure that the dynamic pressure (Q) remains within a range of $\pm$2% of the target value from run to run ($\pm$20 Pa, 95% confidence value). The bias uncertainty of Q is 0.15% and therefore over this $\pm$20 Pa range the uncertainty is on the order of $\pm$0.03 Pa. For cases with ΔF_D on the order of 20% of $F_{D,1}$ or smaller (the vast majority of test results), the second term in Equation 2.20 is approximately four orders of magnitude smaller than the first term, and therefore can be neglected.

Therefore, based on the above order-of-magnitude analysis, the uncertainty estimate for ΔC_D values that accounts for correlated-bias uncertainties between two test runs uses the following bias-error estimation:

$$\delta^2_{\Delta C_D} = \left[\frac{1}{QA}\delta_{\Delta D}\right]^2 \tag{2.21}$$

In the current test program, one model configuration was tested three times over a two-day period, providing a data set to calculate the random uncertainty associated with measurement error and repeatability error. Based on the bias-error quantifications described above and the random uncertainty from this set of test data, the estimated uncertainties for the current test program are listed in Table 2.5. Typical drag-coefficient uncertainties for this type of testing are on the order of 0.002 to 0.003. The higher uncertainties here are associated with the lower test speed (40 m/s instead of the usual 50 m/s) which results in drag loads and dynamics pressures about 1/3 lower that at the higher speed.

Uncertainties associated with the other force and moment coefficients have been calculated, but not documented explicitly here. Error bars are provided in associated graphs.

Table 2.5: Estimated uncertainties for drag-coefficient and drag-area variables (95% confidence levels).

Parameter	**Uncertainty estimate**		
	Bias	Random	Total
C_D	± 0.0025	± 0.0039	± 0.0046
ΔC_D	± 0.0015	± 0.0039	± 0.0042
WAC_D	± 0.0025	± 0.0025	± 0.0035
ΔWAC_D	± 0.0015	± 0.0025	± 0.0029
$C_D A$	± 0.027 m^2	± 0.042 m^2	± 0.049 m^2
$\Delta C_D A$	± 0.016 m^2	± 0.042 m^2	± 0.045 m^2
$WAC_D A$	± 0.027 m^2	± 0.027 m^2	± 0.038 m^2
$\Delta WAC_D A$	± 0.016 m^2	± 0.027 m^2	± 0.031 m^2

3. Wind Tunnel Test Results

3.1 Reynolds-number Sensitivity of Results

The current test program was undertaken at a lower wind speed than is typically used for model-scale HDV testing in the 9 m Wind Tunnel (40 m/s instead of 50 m/s). This was due to the use of the RT^{2}S for the wake-effects part of the test program that was commissioned at the lower test speed. To examine the potential impact of testing at a lower wind speed, speed sweeps were undertaken for the zero-emission-cab and conventional-sleeper-cab models to examine the Reynolds-number sensitivity of the models. Reynolds number (Re) is a non-dimensional parameter representing the ratio of inertial-to-viscous wind forces in the flow around a body, defined here as:

$$Re = \frac{U\,W}{\nu} \tag{3.1}$$

where U is the wind speed relative to the vehicle, W is the vehicle width, and ν is the kinematic viscosity of the air. Ideally, model-scale testing should be conducted at the same Reynolds number as the full-scale vehicle to match the relative flow conditions. However, this is not always possible but equivalence can be assessed by the change in force or moment coefficients with wind speed. Figure 3.1 shows the drag-coefficient results of the speed sweeps conducted for the two tractor-model configurations, without cross winds.

The speed-sweep results of Figure 3.1 show that, for both tractor shapes, the drag coefficient continuously decreases with Reynold-number up to the maximum value of 2.6×10^6, achieved

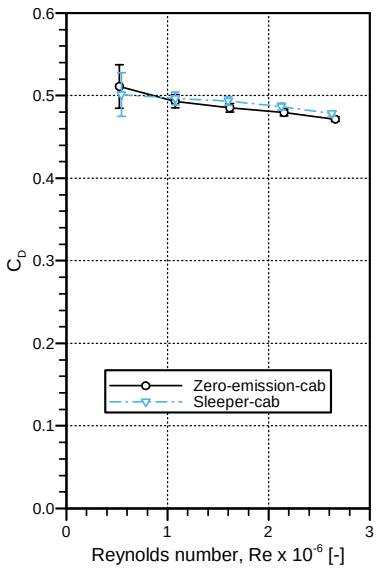

Figure 3.1: Variation of drag coefficient with Reynolds number for two tractor-model configurations, paired with the dry-van-trailer model with side-skirts installed.

at a wind speed of 50 m/s. A full-scale vehicle travelling at highway speed (105 km/h, 65 mph) operates at a Reynolds number of about 5×10^6, about twice the maximum value achieved in these tests. Various studies of commercial-vehicle aerodynamics (Leuschen, 2013, Wood, 2015) suggest that, for shapes like those tested here, Reynolds-number insensitivity of C_D is reached for $Re \geq 3 \times 10^6$. Based on data presented from those other studies, it has been estimated that, at 50 m/s, the drag coefficients measured with the current setup are within about 1% of the equivalent values at highway-conditions. For the selected test speed of 40 m/s ($Re \approx 2.1 \times 10^6$), this assumption means that the measured drag coefficients are expected to be about 3% higher than the corresponding highway-condition values. In addition, the similarity in Reynolds-number sensitivity in Figure 3.1 between the two configurations suggests that differences between tractor shapes measured in the current study can be reasonably assumed to represent differences encountered at highway condition.

3.2 Aerodynamic Improvements from a ZEHDV Shape

The zero-emission-cab tractor model was tested with three variations of the dry-van trailer model, and compared to results for the day-cab- and sleeper-cab-tractor models with the same three trailer configurations. For the purpose of the current study, related to energy savings via aerodynamic improvements, only the drag coefficient results are presented here. The full data sets, including the three force coefficients (drag, side, and lift) and three moment coefficients (rolling, pitching, and yawing), are presented in Appendix A. Figure 3.2 shows the drag-coefficient results for the three tractor configurations and three trailer configurations, as a function of the yaw-angle setting in the wind tunnel, with each sub plot representing a specific trailer configuration. In general, regardless of tractor-trailer configuration, the drag coefficient is a minimum at zero yaw angle, representing no-cross-wind conditions, and increases with greater cross winds from either side. Increases in C_D of about 20% to 45% above the zero-yaw values are observed in the data up to $\pm15^\circ$ yaw angle. Yaw asymmetry is observed in all the data, with higher drag coefficients measured at negative yaw angles compared to the equivalent positive yaw angles. This is a result of either lateral asymmetries in the tractor-and-trailer chassis/shape or non-uniformity of the flow across the test section, or likely a combination of both. The day-cab and zero-emission-cab results show a greater level of yaw-asymmetry than the sleeper-cab results, suggesting model-shape asymmetry is a contributing factor.

Figure 3.2 demonstrates that the zero-emission-cab and sleeper-cab have similar magnitudes of drag coefficient, which are lower than the day-cab tractor. Sleeper-cab tractors generally have lower aerodynamic drag than day-cabs due to their longer shape, which provides greater opportunity for streamlining and minimizing higher pressure over the front surfaces of the vehicle. The changes made to the day-cab-tractor to convert it to the zero-mission-cab configuration demonstrate the potential for improved streamlining of conventional heavy-truck shapes. The drag reduction observed here is assumed to be a results of the streamlining strategy used to develop its shape, that being:

- minimize the extent of surfaces that are perpendicular, or near-perpendicular, to the wind such as the wind-shield region;

- increase the corner radius of the edges at the front of the vehicle to provide a greater forward-projection of surfaces with low-pressure; and
- reduce cooling drag by limiting airflow through the engine bay.

Previous tests with the NRC ProStar-based sleeper-cab tractor variant showed that cooling drag is on the order of $C_D = 0.007$ (approximately a symbol height in the plots) and is therefore assumed to not be a major cause for the reduction in drag from the day-cab to zero-emission-cab models. The changes are thus a result of the first two aspects of the strategy. Given the single-iteration change in its shape, it is unclear whether one of those drag-reduction mechanisms is dominant over the other.

Of particular note for the results of Figure 3.2 is the comparison between the zero-emission-cab shape and the sleeper-cab shape for different trailer configurations. For the standard trailer, both show nearly identical drag coefficients at any given yaw angle, despite the slight yaw-asymmetry differences between the two. While, for the trailer with skirts and tail, the zero-emission cab exhibits lower aerodynamic drag than the sleeper-cab at the lower-magnitude yaw angles (within about $\pm 5°$). This gradual separation of the zero-emission-cab data from the sleeper-cab data from left to right in Figure 3.2 suggests that the beneficial changes to the tractor shape have an influence on the drag-reduction potential of both the side-skirts and boat-tail.

The changes made to the day-cab model to create the zero-emission-cab shape are general enough that the same approach can be applied to the sleeper-cab shape. Although drag reductions are expected from doing this, it is unclear whether the magnitude will be the same, or will be higher or lower for the different cab length. Additional data are required.

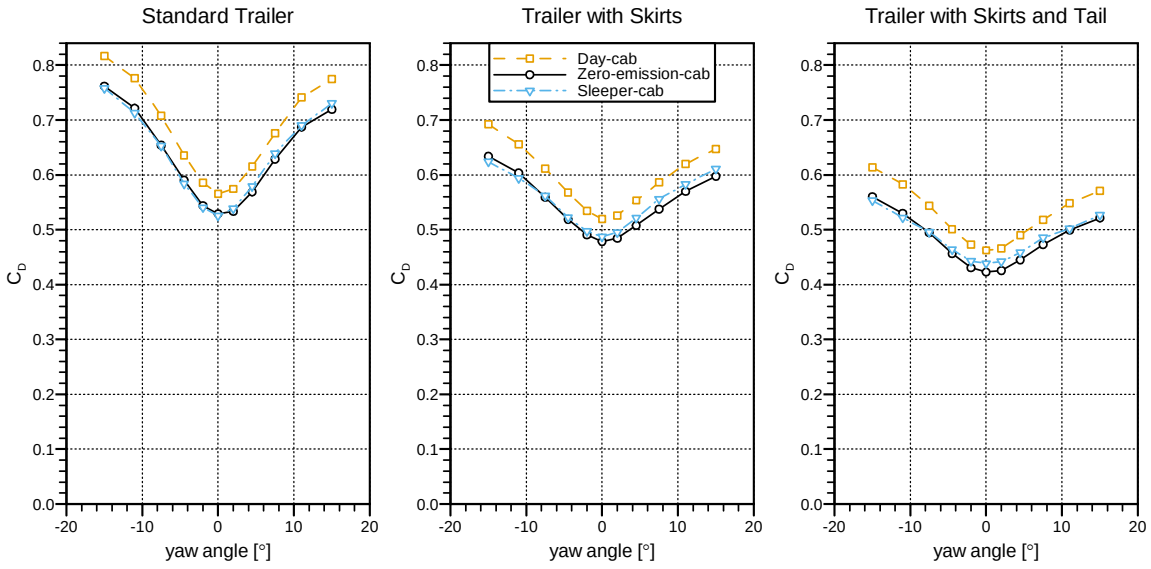

Figure 3.2: Variation of drag coefficient with yaw angle for the three tractor-model configurations paired with the three dry-van-trailer-model configurations. Measurement uncertainty is $\delta C_D = \pm 0.004$, which is smaller than the height of the symbols.

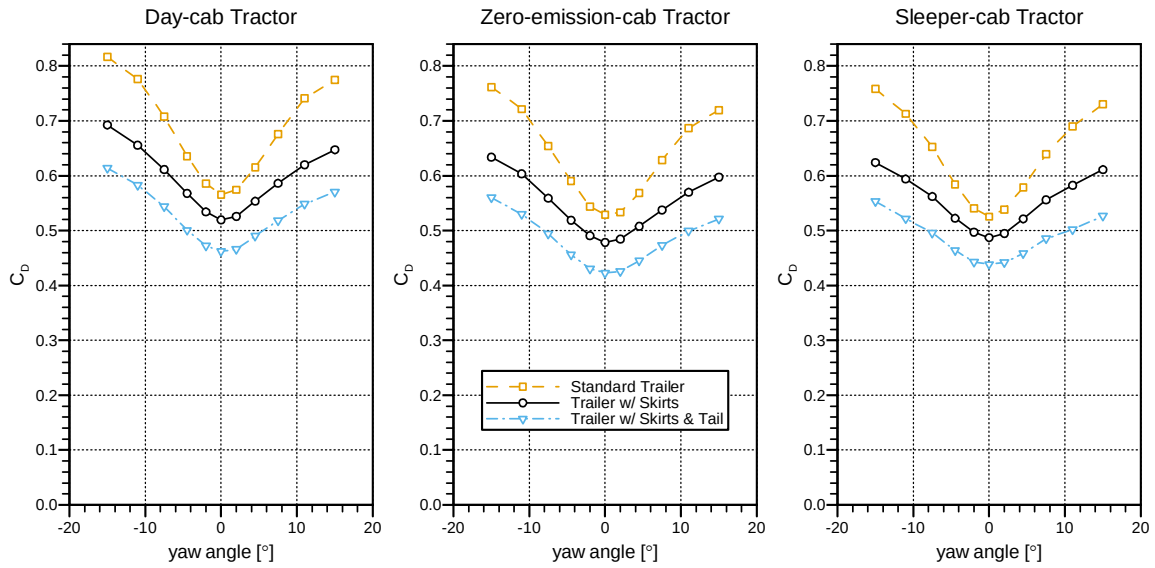

Figure 3.3: Variation of drag coefficient with yaw angle for the three trailer-model configurations paired with the three tractor-model configurations. Measurement uncertainty is $\delta C_D = \pm 0.004$, which is smaller than the height of the symbols.

Figure 3.3 shows the same data as Figure 3.2 but with each sub plot representing a different tractor shape, and thus highlighting the differences in trailer configuration. In general, and as observed in previous studies, trailer technologies such as side-skirts and boat-tails are effective at reducing the drag of HDVs by measurable quantities, on the order of 10% for each of these two technologies.

To provide a quantitative assessment of the aerodynamic drag for the various tractor and trailer configurations, Table 3.1 lists the wind-averaged drag coefficient and drag-area values for all nine test configurations. The data of Table 3.1 represent wind-averaged calculations using the EPA 2-point method (see Section 2.4.4), defined to represent 65 mph road speed (105 km/h). Appendix B provides the corresponding values for the SAE/Mean-wind method and for the Full-wind method that accounts for the probability distribution of the wind speed.

Table 3.1: Wind-averaged drag-coefficient and full-scale drag-area results for the tractor-trailer combinations tested, based on the EPA 2-point method. Uncertainties are $\delta WAC_D = \pm 0.004$ and $\delta WAC_D A = \pm 0.04$ m^2.

Tractor Shape	**Standard Trailer**		**Trailer w/ Skirts**		**Trailer w/ Skirts & Tail**	
	WAC_D [-]	$WAC_D A$ [m^2]	WAC_D [-]	$WAC_D A$ [m^2]	WAC_D [-]	$WAC_D A$ [m^2]
Day-cab	0.625	6.67	0.561	5.98	0.495	5.29
Zero-emission-cab	0.580	6.19	0.513	5.48	0.451	4.81
Sleeper-cab	0.581	6.20	0.522	5.57	0.461	4.92

For each of these vehicle configurations in uniform-flow conditions, the three wind-averaging methods provide approximately the same value, within 1% of each other, while the estimated uncertainty of each value is approximately 0.5%, thus indicating that the three methods are measurably different. The data in Table 3.1 demonstrate the trends observed from Figures 3.2 and 3.3, with the zero-emission-cab and sleeper-cab tractors showing similar drag that is significantly lower than the day-cab tractor, and with large drag reductions associated with adding side-skirts and a boat-tail to the trailer model. To examine more specifically the quantitative changes in aerodynamic drag associated with changes to the tractor and trailer, the difference calculations are provided in Tables 3.2 and 3.3 for the tractor and trailer changes, respectively.

Table 3.2 documents the change in wind-averaged values associated with changing the tractor from the day-cab configuration to either the zero-emission-cab or sleeper-cab configurations. The zero-emission cab exhibits a similar change of magnitude in drag coefficient or drag area regardless of the trailer configuration, while the sleeper cab demonstrates a lower drag-reduction magnitude for the lower-drag trailer configurations. However, despite the reduced magnitude, the sleeper-cab shows a near-constant percentage reduction for the three trailer configurations. These trends suggest that, despite both cab shapes providing lower drag than the day-cab, each are manipulating the drag mechanisms of the overall vehicle differently.

Examining the trailer-device drag-reduction trends in Table 3.3, the differences in drag behaviour noted above emerge as a different trend. Here, it is observed that the magnitude of device drag reduction, either side-skirts alone or skirts-skirts combined with a boat-tail, remains constant between the day-cab and zero-emission-cab tractors, while a lower magnitude is observed for the sleeper-cab tractor. However, the percentage drag change associated with the trailer devices remains the same for the day-cab and sleeper-cab tractor, with higher percentage changes for the zero-emission cab. These results suggest that the interactions between drag changes on the tractor and the trailer differ based on the manner in which tractor drag is reduced. Previous testing at NRC, both for internal research and proprietary client testing, has shown that trailer-device performance magnitude depends on the tractor configuration, with improved performance when using higher-drag tractor configurations, similar to what is seen here between the day-cab and sleeper-cab results.

The zero-emission-cab results here highlight that trailer-aerodynamic improvements can be maintained with a lower-drag tractor, providing evidence that design optimization of tractor-trailer configurations may yield improved energy-use and GHG-emission reductions for HDVs, albeit with a much greater logistical challenge to keep particular tractors and trailers paired in real-world operations. Reasons for the different drag-reduction behaviour observed here may relate to the length of the tractor and/or the design of the lower regions of the tractor.

To conclude the discussion of the zero-emission-cab shape improvements, the changes in drag performance can be related to the tractor aerodynamic-performance metrics defined by the EPA *Greenhouse Gas Emissions Standards and Fuel Efficiency Standards for Medium- and Heavy-Duty Engines and Vehicles - Phase 2* (U.S. EPA and U.S. DOT, 2016). Although zero-emission HDVs are not necessarily regulated by these rules, the aerodynamic performance metrics can be used as indicators of improvement, especially if conventional internal-combustion vehicles follow similar shaping strategies. Under an assumption that these wind-tunnel results corre-

Table 3.2: Change in wind-averaged drag-coefficient and full-scale drag-area results for different tractor configurations, based on the EPA 2-point method. Uncertainties are $\delta\Delta WAC_D = \pm 0.003$ and $\delta\Delta WAC_DA = \pm 0.03$ m^2.

Tractor Change	**Standard Trailer**			**Trailer w/ Skirts**			**Trailer w/ Skirts & Tail**		
	ΔWAC_D [-]	ΔWAC_DA [m^2]	Δ [%]	ΔWAC_D [-]	ΔWAC_DA [m^2]	Δ [%]	ΔWAC_D [-]	ΔWAC_DA [m^2]	Δ [%]
Day-cab to Zero-emission-cab	-0.046	-0.49	-7.3	-0.047	-0.51	-8.4	-0.045	-0.48	-9.1
Day-cab to Sleeper-cab	-0.044	-0.47	-7.0	-0.039	-0.41	-6.9	-0.034	-0.37	-6.9

Table 3.3: Change in wind-averaged drag-coefficient and full-scale drag-area results for different trailer configurations, based on the EPA 2-point method. Uncertainties are $\delta\Delta WAC_D = \pm 0.003$ and $\delta\Delta WAC_DA = \pm 0.03$ m^2.

Trailer Change	**Day-cab Tractor**			**Zero-emission-cab Tractor**			**Sleeper-cab Tractor**		
	ΔWAC_D [-]	ΔWAC_DA [m^2]	Δ [%]	ΔWAC_D [-]	ΔWAC_DA [m^2]	Δ [%]	ΔWAC_D [-]	ΔWAC_DA [m^2]	Δ [%]
Add Skirts	-0.065	-0.69	-10.3	-0.066	-0.71	-11.4	-0.059	-0.63	-10.2
Add Skirts & Tail	-0.130	-1.39	-20.8	-0.129	-1.38	-22.3	-0.120	-1.28	-20.7

late reasonably well to the reference coast-down method for wind-averaged drag-area reporting (unpublished work suggests this to be accurate to within 3%), and that the NRC side-skirts perform the same as the EPA-defined side-skirt shape (other unpublished work showed this to be true within the experimental uncertainty), then the full-scale drag-area-reduction of 0.5 m^2 demonstrated here can be assumed to be appropriate for comparison purposes. For high-roof day-cab or sleeper-cab tractors paired with 53 ft dry-van trailers, most aerodynamic-bin increments are 0.5 m^2, equivalent to the zero-emission-cab improvement demonstrated here. Given that the shape-change implemented here is a first attempt without any optimization procedure, it is conceivable that improvements of greater than one bin level are possible.

3.3 Aerodynamic Influence of Mirrors

Mirrors are a recognized noticeable source of drag on an HDV. However, they are required for safety purposes. The potential to reduce the size of mirrors exists within current safety regulations (Patten *et al.*, 2012), while the removal of mirrors and replacement with low-profile camera systems is not yet permitted in Canada or the United States. Wind-tunnel tests were conducted for two tractor configurations, the day-cab and zero-emission-cab tractors, to quantify the changes in aerodynamic drag associated with the addition of fender mirrors and the removal of all mirrors. Photographs of the tractor models with and without these mirror models are provided in Figure 2.11. For all mirror tests, the trailer was configured with the NRC side-skirts.

The test results are shown in Figure 3.4. Due to project-budget constraints, only the positive-yaw-angle range was tested for the day-cab-tractor configuration. The results show that, for both tractors, the drag increases when fender mirrors are added, and the drag decreases when mirrors are removed. The main mirrors show a greater drag reduction when removed, than the increase associated with adding the fender mirrors. Referring back to Figure 2.11, the fender mirrors have a smaller frontal area than the main mirrors, which is the principal reason for their lower drag changes. Of particular interest, when comparing the effects of mirrors on the two tractor shapes, removing the main mirrors from the zero-emission cab shows a constant change regardless of yaw angle, while the day-cab results show greater drag reduction at low yaw angles than at high yaw angles. This may be due to the relative position of the main mirrors to the front surfaces of the cab models, with the mirrors "further back" on the zero-emission cab due to its more forward windscreen region. For zero-emission tractors, the driver may be positioned more forward and the fender mirror used here may be more appropriate as main mirror locations.

To provide quantitative results, Table 3.4 lists the wind-averaged drag-coefficient and drag-area values for the two tractor models with the three mirror configurations tested for each. Of greater pertinence is Table 3.5 that provides the changes in drag-coefficient and drag-area based on the measurements. The results show that the fender mirrors add approximately 1% drag to the vehicle, while removing the main mirrors reduces the drag by approximately 3%. Although differences in the tabulated values are observed between the day-cab and zero-emission-cab models, the uncertainty bounds overlap and thus differences cannot be concluded.

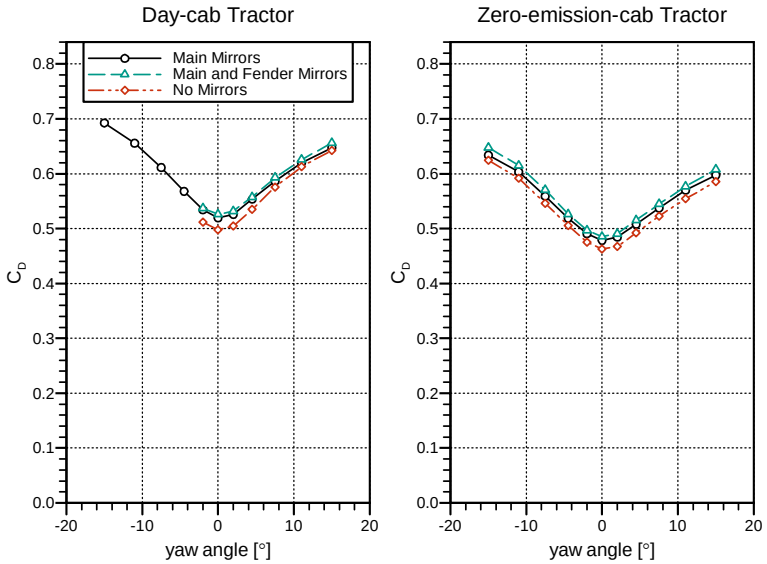

Figure 3.4: Variation of drag coefficient with yaw angle for the three mirror configurations paired with the two tractor-model configurations. Measurement uncertainty is $\delta C_D = \pm 0.004$, which is smaller than the height of the symbols.

Table 3.4: Wind-averaged drag-coefficient and full-scale drag-area results for different mirror configurations tested, based on the EPA 2-point method. Uncertainties are $\delta WAC_D = \pm 0.004$ and $\delta WAC_D A = \pm 0.04$ m^2. * Day-cab results are for positive yaw-angle range only.

Tractor Shape	**Main Mirrors**		**Main + Fender Mirrors**		**No Mirrors**	
	WAC_D [-]	$WAC_D A$ [m^2]	WAC_D [-]	$WAC_D A$ [m^2]	WAC_D [-]	$WAC_D A$ [m^2]
Day-cab *	0.553	5.90	0.558	5.95	0.535	5.71
Zero-emission-cab	0.513	5.48	0.521	5.56	0.499	5.33

Table 3.5: Change in wind-averaged drag-coefficient and full-scale drag-area results for changes in mirrors, based on the EPA 2-point method. Uncertainties are $\delta \Delta WAC_D = \pm 0.003$ and $\delta \Delta WAC_D A = \pm 0.03$ m^2. * Day-cab results are for positive yaw-angle range only.

Mirror Change	**Day-cab Tractor ***			**Zero-emission-cab Tractor**		
	ΔWAC_D [-]	$\Delta WAC_D A$ [m^2]	Δ [%]	ΔWAC_D [-]	$\Delta WAC_D A$ [m^2]	Δ [%]
Add Fender Mirrors	+0.004	+0.05	+0.8	+0.008	+0.08	+1.5
Remove Mirrors	-0.019	-0.20	-3.4	-0.014	-0.15	-2.8

Table 3.6: Estimates from other NRC-based studies of mirror addition/removal, based on the SAE Mean-Wind method or single-C_D value. Uncertainties are not quantified for these results.

Test Description	Main Mirrors		Fender Mirrors	
	ΔWAC_D [-]	$\Delta WAC_D A$ [m^2]	ΔWAC_D [-]	$\Delta WAC_D A$ [m^2]
Full-Scale Truck in 9 m Wind Tunnel (Leuschen and Cooper, 2006)	-0.016	+0.17	+0.010	+0.10
30%-scale Truck in 9 m Wind Tunnel (unpublished)	-0.020	-0.21	+0.007	+0.08

To provide some further context to these measurements, and their wider applicability, Table 3.6 provides estimates the wind-averaged drag-coefficient and drag-area performance of the same main and fender mirror changes measured from other studies in the NRC 9 m Wind Tunnel. Leuschen and Cooper (2006) performed a full-scale truck study using a Volvo VNL tractor and removed the stock fender and main mirrors. In 2016, the sleeper-cab variant of the 30%-scale adapted-ProStar model was tested with and without the same main and fender mirror models used in the current study. Both previous studies measured mirror-related drag changes of similar magnitude to those in the current study. The main mirrors in all of these studies, including the current study, are not necessarily representative of the most modern HDV mirrors. Some modern mirrors have only a single support post, on the bottom, like that of the Kenworth T680 sleeper-cab tractor of the current study, and like the current International LT (the modern version of the ProStar), the Freightliner Cascadia, and the Peterbilt 579. A single support-post configuration is expected to provide lower drag than the double-mount (top and bottom) concept tested here.

3.4 Aerodynamic Influence of Traffic Wakes on a ZEHDV Shape

Current research activities at NRC include the investigation of traffic effects on the aerodynamics of road vehicles, in collaboration with the TC eTV program. A 30%-scale version of the NRC Road Traffic and Turbulence System (RT^{2}S) was build and used for the current test campaign, as part of the larger research project undertaken at the time. Although a separate report will document all the traffic-wake test results and provide a greater level of discussion surrounding the results (McAuliffe *et al.*, 2022), the measurements performed using the zero-emission-cab tractor are presented here to document an important influence when considering the aerodynamic performance of HDVs in real-world conditions. As described in Section 2.1.5, the RT^{2}S simulated the wakes of numerous traffic scenarios, including different vehicle types (a single CAR, a single SUV, a single HDV, and Mixed LDV traffic), representing vehicles in the same and/or the adjacent lane, at various effective distances of 25 m up to 100 m, and under a range of cross winds with yaw angles up to 11°. Over 40 unique wake scenarios were tested.

Figure 3.5 shows the drag-coefficient result of these wake-condition tests, along with the corresponding uniform-flow results, for the zero-emission-cab tractor model paired with the dry-

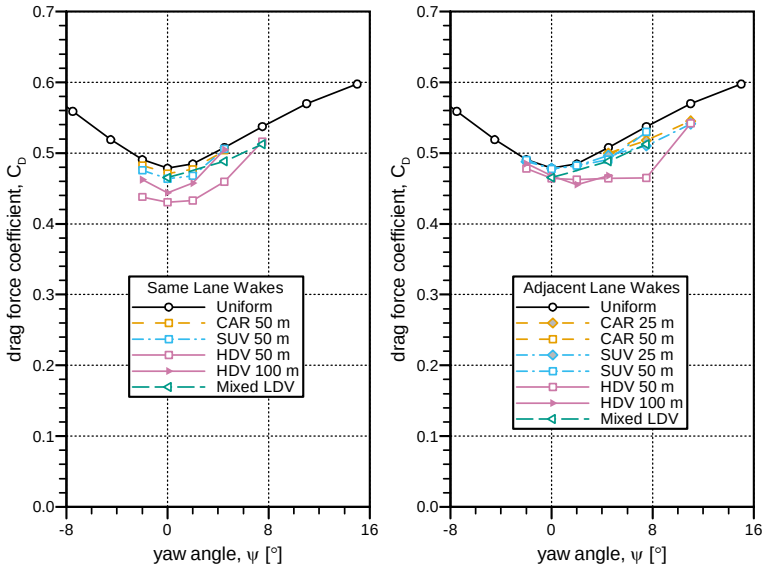

Figure 3.5: Variation of drag coefficient with yaw angle for uniform- and wake-flow results measured with the zero-emission-cab tractor with the dry-van-trailer model outfitted with side-skirts. Left) traffic wake-conditions with same-lane vehicles. Right) traffic wake-conditions with adjacent-lane vehicles. Measurement uncertainty is $\delta C_D = \pm 0.004$, which is approximately the height of the symbols.

van-trailer model outfitted with side-skirts. The left plot shows the results with vehicles effectively in the same lane as the HDV, and the right plot has data with vehicles in the adjacent lane. Same-lane results were expected to be symmetric with yaw angle, about zero, so only negative yaw angles to -2° were tested. Here, positive yaw angles have winds coming from the driver side towards the passenger side, and the adjacent lane location has vehicle effectively in a lane to the left (driver side) of the HDV. This leads to wakes propagating into the HDV lane under positive-yaw-angle conditions. The Mixed LDV results are shown in both plots because it represents an on-road scenario with LDVs in the same and adjacent lane. Some basic observations and trends that emerge from the results include:

- Traffic wakes reduce the aerodynamic drag of the HDV;
- Larger vehicles have a larger influence on the HDV drag coefficient;
- Closer vehicle distances have a larger influence on the HDV drag coefficient;
- Larger vehicle distances affect the drag coefficient over a narrower range of yaw angles;
- Adjacent-lane wakes in cross winds can have a larger influence on the HDV drag coefficient than the equivalent same-lane-vehicle wake, particularly for HDV wakes;
- For same-lane conditions, the LDV wake cases (CAR, SUV, Mixed LDV cases) demonstrate drag reductions up to about 4% and the HDV wake cases demonstrate drag reductions up to about 11%; and
- for adjacent-lane conditions, the LDV wake cases (CAR, SUV, Mixed LDV cases) demon-

strate drag reductions up to about 5% and the HDV wake cases demonstrate drag reductions up to about 14%.

To provide some context for how these wake conditions apply in a wind-averaged sense, Table 3.7 provides the calculated wind-averaged drag-coefficient and drag-area values, and the associated percentage reductions compared to uniform conditions, for each of the wake conditions. The calculated results are based on the full-wind method (see Section 2.4.4), which is most appropriate for yaw-asymmetric results. These results show that, despite higher individual drag reductions observed for adjacent-lane wakes in cross winds, when considering the average wind climate, the wakes from same-lane vehicles provide larger wind-averaged-drag reductions. The largest wind-averaged drag reductions are for the HDV-wake, with up to about 8% reduction observed for same-lane conditions and 4% for adjacent-lane conditions. These results show why track-based platooning studies have shown measurable fuel savings at large inter-vehicle distances, up to 87 m and expected beyond (McAuliffe *et al.*, 2018; Lammert *et al.*, 2020; McAuliffe *et al.*, 2020).

The results of Table 3.7 should not be used to make conclusions about traffic effects in general. They are strictly an indicator of the influence of wake effects for these particular scenarios. More work is required to understand the net wake effects encountered on the road, which requires an understanding of traffic-speed, traffic-density, and traffic-spacing distributions. This topic is being addressed as part of the wake-effects project leveraged to conduct the current project, for which a report is currently being prepared (McAuliffe *et al.*, 2022). The important take-away from these results is that the aerodynamic drag of a heavy-duty vehicle is influenced by the wakes of upstream traffic, even for safe inter-vehicle distances.

Table 3.7: Wind-averaged drag-coefficient and drag-area results for the traffic-wake testing conditions, based on the Full-wind method. Uncertainties are $\delta\Delta WAC_D = \pm 0.003$ and $\delta\Delta WAC_D A = \pm 0.03$ m^2.

Flow Condition	**Wakes from Same Lane**			**Wakes from Adjacent Lane**		
	ΔWAC_D [-]	$\Delta WAC_D A$ [m^2]	Δ [%]	ΔWAC_D [-]	$\Delta WAC_D A$ [m^2]	Δ [%]
Uniform Flow	0.517	5.51		0.517	5.51	
CAR 25 m				0.513	5.47	-0.7%
CAR 50 m	0.512	5.46	-0.9%	0.515	5.48	-0.4%
SUV 25 m				0.511	5.45	-1.1%
SUV 50 m	0.509	5.42	-1.6%	0.513	5.47	-0.7%
HDV 50 m	0.474	5.05	-8.3%	0.496	5.29	-4.1%
HDV 100 m	0.501	5.34	-3.0%	0.504	5.37	-2.6%
Mixed LDV	0.507	5.41	-1.9%	0.507	5.41	-1.9%

4. Summary and Conclusions

A project has been initiated to examine the energy-savings and range-extension benefits from aerodynamic improvements to HDVs resulting from emerging ZEHDV tractor shapes. As a preliminary task in the project (Phase 0), a test campaign was undertaken in the NRC 9 m Wind Tunnel using a 30%-scale tractor-trailer model to examine the aerodynamic-drag benefits of HDVs associated with a ZEHDV shape. Three experimental tasks were carried out to examine changes to the aerodynamic drag of HDV and ZEHDV shapes for: 1) combinations of three different tractor and three different trailer configurations; 2) the addition of fender mirrors to, or the removal of main mirrors from, two tractor shapes; and 3) different flow conditions representing the wakes of various upstream-traffic conditions.

Drag-coefficient and drag-area results show that changes to the shape of a day-cab tractor, based on aerodynamic considerations to represent emerging ZEHDV shapes, reduced the aerodynamic drag-area of the vehicle by 7-9%, representing about one EPA bin level (0.5 m^2). The results further show that aerodynamic improvement of the ZEHDV shape demonstrated less sensitivity to trailer configuration than did the conventional day-cab and sleeper-cab shapes. Conversely, this demonstrates that trailer-device performance was less sensitive to the ZEHDV shape than to the conventional shapes. These outcomes suggest that, with reasonable efforts to optimize the shape of HDVs based on new drivetrain/chassis architectures, significant energy savings from aerodynamic improvements are possible over conventional North-American HDV shapes.

The main- and fender-mirror test results showed that drag reductions on the order of 4% are possible with the removal of all mirrors from an HDV tractor. Drag changes of 1-2% were documented for fender mirrors, and 3% for main mirrors. These results suggest that reducing mirror size, or replacing mirrors with low-drag camera-based rear-view systems, can provide measurable energy savings for long-haul HDV applications.

The wake-effects testing, documented strictly for the ZEHDV model here, showed that the model experienced reduced aerodynamic drag in excess of 10% when exposed to the wakes of the specific forward-traffic conditions examined, which represent safe driving distances, even with traffic in an adjacent lane. These results provide some additional evidence that HDVs are experiencing the aerodynamic platooning effect in everyday traffic. The reduced aerodynamic drag from traffic-wake conditions suggests that current estimates of GHG emissions via tools like the EPA Greenhouse-gas Emission Model (GEM) may not consider the lower drag of HDVs when driving in traffic, and may therefore be overestimating GHG reductions from aerodynamic technologies/improvements via $C_D A$ values measured or assessed for isolated driving conditions.

The results presented in this report regarding the drag reduction associated with one new concept should be considered a precursory study. The findings provide a basis for next steps in examining the potential benefits of emerging ZEHDV shapes. Phases 1 and 2 of the project will examine this potential via a simulation-based shape-optimization study, followed by wind-tunnel testing of viable concepts, and subsequent analysis of the energy savings and range

extension possible from these concepts in different operating environments ranging from first-mile/last-mile delivery to long-haul operations.

References

Barlow, J. B., Rae, W. H. and Pope, A. (1999), *Low-Speed Wind Tunnel Testing*, 3rd ed., Wiley-Interscience.

Buckley, F. J., Marks, C. and Walston, W. J. (1978), "Study of aerodynamic methods for improving truck fuel economy," Technical Report No. PB-80-101272.

Clark, C. (2010), "A Study of the flow conditions for ground-vehicle testing in the 9 m x 9 m wind tunnel facility with the GESS installed," NRC Report No. LTR-AL-2010-0022, *National Research Council Canada*.

EPA (2015), "EPA SmartWay Verification Test Procedure for Determining Fuel Savings: Scale Wind Tunnels," Version 1 , *U.S. Environmental Protection Agency*.

Kirchhefer, A. J. (2017), "Flow Angularity in the NRC 9 m WindTunnel," NRC Report No. LTR-AL-2016-0004.

Kirchhefer, A. J. and McAuliffe, B. R. (2016), "NRC Trailer Skirts - SmartWay Verification Testing using the NRC 9 m Wind Tunnel - Final Report," NRC Report No. LTR-AL-2016-0009-V4, *National Research Council Canada*.

Lammert, M. P., McAuliffe, B. R., Raeesi, A., Smith, P., Hoffman, M. and Bevly, D. (2020), "Impact of Lateral Alignment on the Energy Savings of a Truck Platoon," SAE Paper No. 2020-01-0594.

Leuschen, J. (2013), "Considerations for the Wind Tunnel Simulation of Tractor-Trailer Combinations: Correlation of Full- and Half-Scale Measurements," SAE Int. J. Commer. Veh., **6(2),** doi:10.4271/2013-01-2456.

Leuschen, J. and Cooper, K. R. (2006), "Full-Scale Wind Tunnel Tests of Production and Prototype, Second-Generation Aerodynamic Drag-Reduction Devices for Tractor-Trailers," SAE Paper No. 2006-01-3456.

McAuliffe, B. R., Barber, H. and Ghorbanishohrat, F. (2022), "Aerodynamics of Road Vehicles in Real-world Conditions - Progress Report - Traffic Aerodynamics Phases 4," NRC Report No. LTR-AL-2022-0070.

McAuliffe, B. R. and D'Auteuil, A. (2016), "A System for Simulating Road-Representative Atmospheric Turbulence for Ground Vehicles in a Large Wind Tunnel," SAE Int. J. Passeng. Cars - Mech. Syst., **9(2),** doi: 10.4271/2014-01-2451.

McAuliffe, B. R., Lammert, M., Lu, X., Shladover, S., Surcel, M. and Kailas, A. (2018), "Influences on Energy Savings of Heavy Trucks Using Cooperative Adaptive Cruise Control," SAE Paper No. 2018-01-1181.

McAuliffe, B. R., Raeesi, A., Lammert, M. P., Smith, P., Hoffman, M. and Bevly, D. (2020), "Impact of Mixed Traffic on the Energy Savings of a Truck Platoon," SAE Paper No. 2020-01-0679.

McAuliffe, B. R., Sowmianarayanan, B. and Barber, H. (2021*a*), "Near-to-Far Wake Characteristics of Road Vehicles Part 1: Influence of Ground Motion and Vehicle Shape," SAE Int. J. Advances & Curr. Prac. in Mobility, **3(4):2009-2024,** doi: 10.4271/2021-01-0957.

McAuliffe, B. R., Sowmianarayanan, B. and Barber, H. (2021*b*), "Near-to-Far Wake Characteristics of Road Vehicles Part 2: Influence of Freestream Turbulence and Cross Winds," SAE Int. J. Advances & Curr. Prac. in Mobility, **3(4):2025-2045,** doi: 10.4271/2021-01-0949.

McAuliffe, B. R., Sowmianarayanan, B. and Barber, H. (2021*c*), "Near-to-Far Wake Characteristics of Road Vehicles Part 3: Influence of Multi-Vehicle Interactions," SAE Int. J. Advances & Curr. Prac. in Mobility, **3(4):2046-2068,** doi: 10.4271/2021-01-0959.

McAuliffe, B. R. and Wall, A. (2016), "Aerodynamic Performance of Flat-Panel Boat-Tails and Their Interactive Benefits with Side-Skirts," SAE Int. J. Commer. Veh., **9(2),** doi: 10.4271/2016-01-8015.

McTavish, S. and McAuliffe, B. R. (2021), "Improved aerodynamic fuel savings predictions for heavy-duty vehiclesusing route-specific wind simulations," Journal of Wind Engineering & Industrial Aerodynamics, **210,** https://doi.org/10.1016/j.jweia.2021.104528.

National Academy of Sciences (2010), "Technologies and Approaches to Reducing the Fuel Consumption of Medium- and Heavy-Duty Vehicles," Committee to Assess Fuel Economy Technologies for Medium- and Heavy-Duty Vehicles, DOI: 10.17226/12845 , *National Academy of Sciences*.

Patten, J., McAuliffe, B. R., Mayda, W. and Tanguay, B. (2012), "Review of Aerodynamic Drag Reduction Devices for Heavy Trucks and Buses," Report No. CSTT-HVC-TR-205.

SAE J1252 (2012), "SAE Wind Tunnel Test Procedure for Trucks and Busses," Surface Vehicle Recommended Practice No. J1252.

SAE SP-1176 (1996), "Closed-Test-Section Wind Tunnel Blockage Corrections for Road Vehicles," SAE Special Publication No. SP-1176, *SAE International*.

U.S. EPA and U.S. DOT (2016), "Greenhouse Gas Emissions Standards and Fuel Efficiency Standards for Medium- and Heavy-Duty Engines and Vehicles - Phase 2," US Federal Register, **81(206)**, pp. 73478–74274.

Wood, R. (2015), "Reynolds Number Impact on Commercial Vehicle Aerodynamics and Performance," SAE Int. J. Commer. Veh., **8(2),** doi: 10.4271/2015-01-2859.

A. Wind Tunnel Measurements

The force- and moment-coefficient measurements for the three tractor-model data sets are presented in Figures A.1 through A.3.

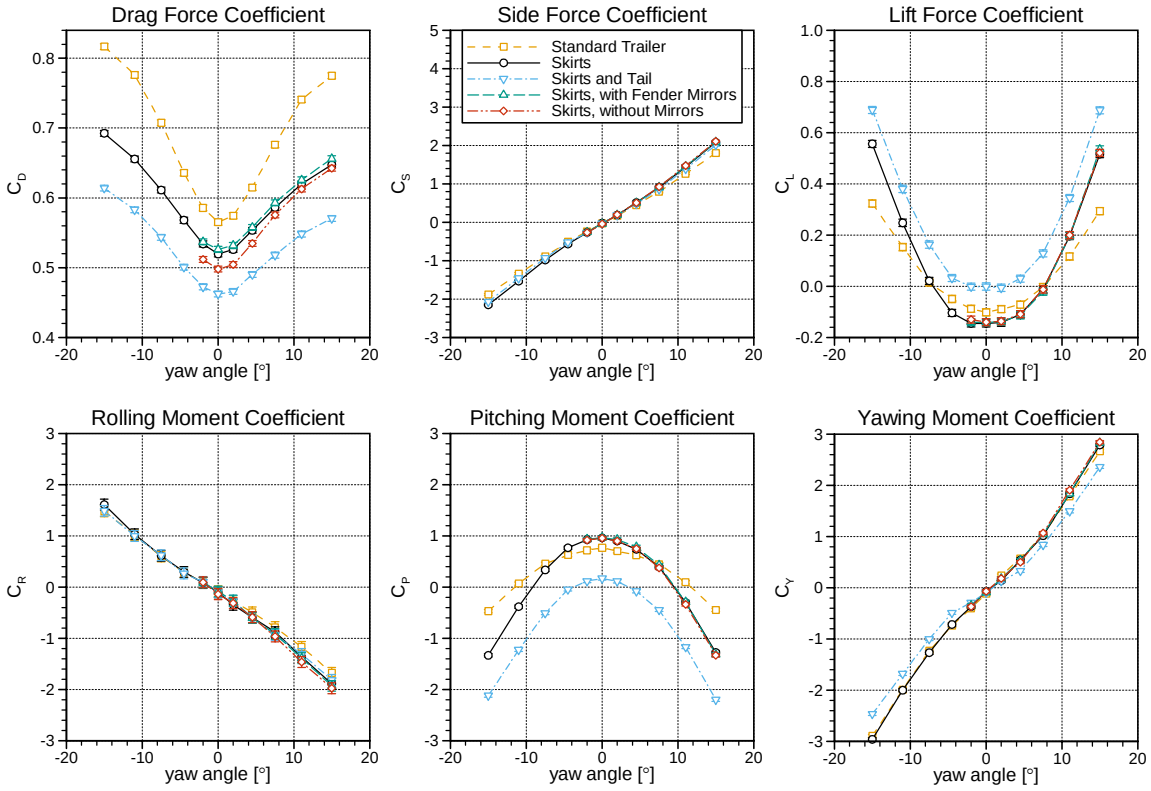

Figure A.1: Variation of force and moment coefficients with yaw angle for all uniform-flow data measured with the day-cab tractor model.

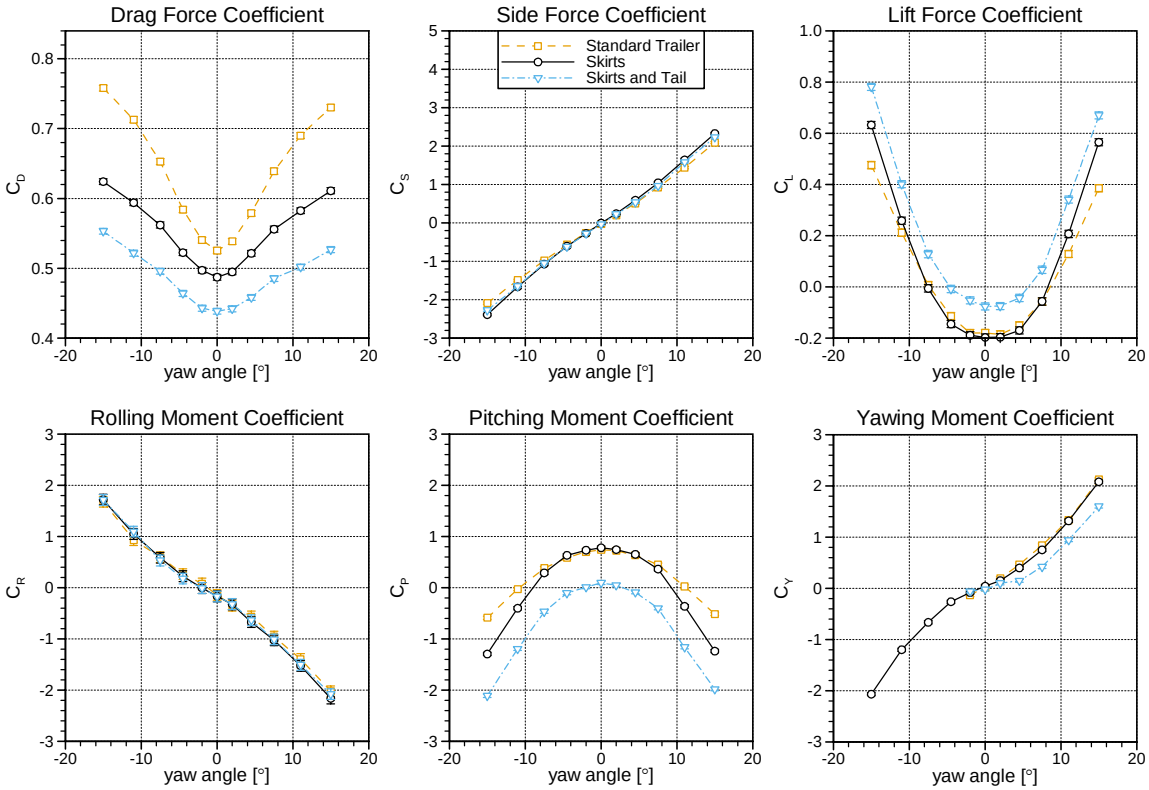

Figure A.2: Variation of force and moment coefficients with yaw angle for all uniform-flow data measured with the sleeper-cab tractor model.

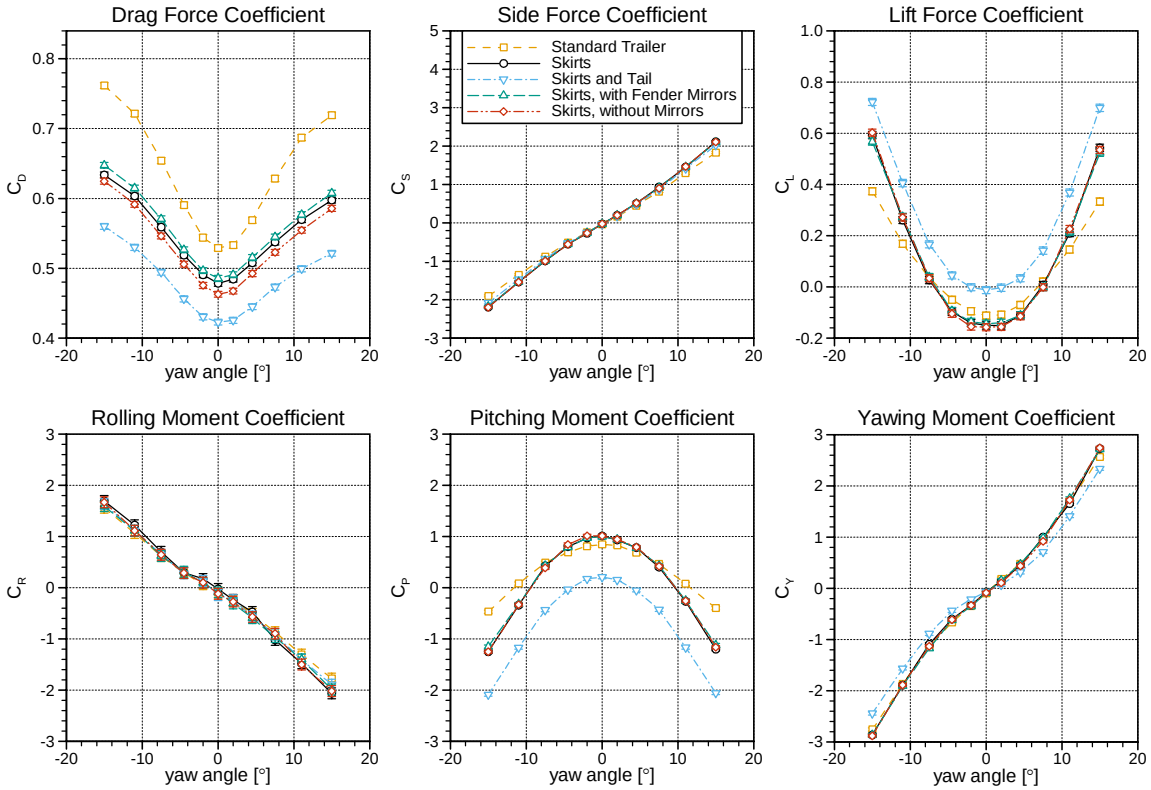

Figure A.3: Variation of force and moment coefficients with yaw angle for all uniform-flow data measured with the zero-emission-cab tractor model.

B. Comparison of Uniform-wind Results Using Different Wind-averaging Methods

Section 2.4.4 documented three methods to calculate a wind-averaged drag-coefficient or drag-area value. The Full-wind method (Section 2.4.4) represents the most general method based on a specified wind distribution, while the Mean-wind method (2.4.4) makes a simplifying assumption that the wind distribution collapses to a single value. The 2-point method (Section 2.4.4) is an approximation to the Mean-wind method, based good correlation between the two. Table B.1 presents the corresponding three values of wind-averaged drag coefficient and wind-averaged drag area for all the uniform-wind test configurations presented in this report. Both the Mean-wind and 2-point methods provide lower wind-averaged values than the Full-wind method, with the 2-point method generally showing greater differences (0.4% to 1.0% lower) than the Mean-wind method (0.2% to 0.7% lower).

Although not explicitly presented here, the application of the three methods to the wake-effects drag-coefficient data for the zero-emission-cab model yields larger differences between the simplified methods and the Full-wind method, with a greater disparity between them. The Full-wind values were presented in Table 3.7. The Mean-wind methods provide values from -1.2% to +0.6% of the Full-wind values, while the 2-point method provides values from -2.0% to +2.1% of the Full-wind values.

Table B.1: Wind-averaged drag-coefficients for all uniform-wind test conditions presented in the report, calculated based on the full-wind, mean-wind, and 2-point methods, representing 105 km/h (65 mph) ground speed. Uncertainties are $\delta WAC_D = \pm 0.004$ and $\delta WAC_D A = \pm 0.04$ m^2.

Model Configuration			Yaw	Drag Coefficient, WAC_D [-]			Drag Area, $WAC_D A$ [m^2]		
Tractor	**Trailer**	**Mirrors**	**Range**	**Full-wind**	**Mean-wind**	**2-point**	**Full-wind**	**Mean-wind**	**2-point**
Zero-emission	Standard	Main	all	0.584	0.580	0.580	6.23	6.19	6.19
	Skirts	Main	all	0.517	0.515	0.513	5.51	5.49	5.48
	Skirts + Tail	Main	all	0.455	0.452	0.451	4.85	4.83	4.81
	Skirts	Main + Fender	all	0.524	0.522	0.521	5.60	5.57	5.56
	Skirts	None	all	0.502	0.500	0.499	5.35	5.33	5.33
Day-cab	Standard	Main	all	0.629	0.625	0.625	6.71	6.67	6.67
	Skirts	Main	all	0.563	0.561	0.561	6.01	5.99	5.98
	Skirts + Tail	Main	all	0.499	0.497	0.495	5.32	5.30	5.29
	Skirts	Main	positive	0.556	0.554	0.553	5.93	5.92	5.90
	Skirts	Main + Fender	positive	0.562	0.560	0.558	6.00	5.97	5.95
	Skirts	None	positive	0.538	0.536	0.535	5.74	5.72	5.71
Sleeper-cab	Standard	Main	all	0.585	0.582	0.581	6.24	6.21	6.20
	Skirts	Main	all	0.525	0.524	0.522	5.61	5.59	5.57
	Skirts + Tail	Main	all	0.466	0.464	0.461	4.97	4.95	4.92